Fibre Optics Approach to Dosimetry

A thesis
submitted in partial fulfilment
of the requirements for the Degree
of
Master of Science in Medical Physics

by

Kaidi Liang

Department of Physics and Astronomy
University of Canterbury
Christchurch, New Zealand
2012

Abstract

Dosimetry is the methodology of determining the amount of radiation energy imparted in matter and volume. Although several techniques and devices are available for use in both laboratory and clinical settings, most rely on certain conditions, assumptions and approximations to convert the energy into radiation dose. The many uncertainties from current techniques are introduced due to the material differences between the sensitive detector volume and the phantom material, typically water.

The aim of this thesis is to use the water sample itself to detect the amount of radiation energy that has been imparted upon it. Radiation energy absorbed by the sample is ultimately converted into heat, raising the temperature of the sample and changing the refractive index property. The refractive index change results in a shortening of the optical path length and as a result, light passing through the sample experiences a phase change. Phase information cannot be directly measured, as it is merely a property of light wave propagation, thus another technique must be used. Digital holographic interferometry was employed to capture snapshots of the sample's changing state over time, and when compared with a reference, the interference phase information was extracted and used to calculate the refractive index change, which can then be related to radiation absorbed dose.

The aim of this research was to design and build interferometry setups using holographic interferometry to determine the refractive index change induced by radiation and to explore the possibilities of using fibre optics. Experiments were conducted on the setups to determine the validity of the method and the accuracy of the system.

With external heating sources in the forms of an open flame and infrared laser, we could see distinct heating patterns formed in the phase images. The phase allowed the calculation of the temperature and therefore energy from the change in refractive index, but was limited to phase differences within 2π between the images, due to wrapped phases. In the stability tests, we demonstrated the accuracy of the system and found it was heavily influenced by the amount of vibration in the vicinity. In the short term, a standard deviation of 0.015 degrees was recorded but a larger standard deviation of 0.078 degrees was measured in the longer term. We can be confident of the temperature measurements to within 0.1 of a degree, equal to hundreds of Grays in radiation dose, however this is not sufficiently accurate for dosimetry. Future work may include improving accuracy by reducing the vibration in the system.

Acknowledgments

Firstly I would like to thank my family, especially my mother, for her support throughout the difficult times. Without their encouragement, I could not have completed this thesis.

I would like to thank and express my deepest gratitude to my supervisors for putting up with me through the last two years:
Dr Frédérique Vanholsbeeck: for always being there and allowing me the opportunity to work in world class facilities at the University of Auckland alongside some of the best optics researchers in the country.
Dr Juergen Meyer: for always being approachable and knowledgeable, working tirelessly to solve problems that are presented.

I would like to thank Alicia Cavan for her willingness to help and share her knowledge and developments; and thanks to Dr Stéphane Coen for his insights and the loan of his camera.

Lastly big thanks to my friends: Neil Campbell for his patience in listening to my complaints and pointing out my mistakes; Jason Kuo for his useful points and colourful (sometimes not practical) lunch ideas.

Contents

List of Figures

Glossary

2D	*two-dimensional*
3D	t*hree-dimensional*
CCD	*charged-coupled device*
DAQ	*data acquisition*
DC	*direct current*
DSLR	*digital single lens reflex (camera)*
Gy	*Grays (Joules per Kilogram)*
He-Ne	*Helium-Neon (laser)*
IR	*infrared*
keV	*kilo-electron volts*
MOSFET	*metal oxide field effect transistor*
MRT	*Microbeam radiation therapy*
OPL	*optical path length*
PVDR	*peak-to-valley dose ratio*

1. Introduction

As the world human population ages, cancer has become a major cause of death[1]. Although many cancers can be treated surgically, less traumatic alternative options such as radiation therapy are becoming more prominent as the technology becomes readily available. Radiation has the unique property of being able to be delivered at a distance and deposit its energy causing ionisations in its path, potentially lethal damage to cells[2]. However radiation does not discriminate the cells it passes through to determine whether they are cancerous or not. Therefore the radiation may damage or kill healthy cells along its path. The aim of radiation therapy is to cause maximum damage to tumourous cells while sparing healthy tissues. The challenge remains to deliver and quantify an accurate dose of radiation to the target tumour. Several dosimetric techniques are available to measure the radiation absorbed dose, but they have limitations[3]. In particular, the non-tissue equivalence of the detector housing and the sensitive volume leads to perturbations of the beam fluence and necessitates correction factors. Another constraint placed on the conventional dosimetric techniques is the limited resolution. This is an issue for small field dosimetry and for measurements in high dose gradient regions. The aim of this project is to develop, as a proof of principle, a fibre optics setup in a lab environment that accurately measures the radiation beam profile and the absolute radiation energy imparted in the given sample based on the change in the refractive index of the sample due to the deposition of radiation dose.

1.1 Brief Overview of Dosimetric Techniques

Dosimetry is the practice of quantitatively determining the energy deposited in a medium by an ionising beam. The quantity of absorbed dose is defined by the amount of energy absorbed per kilogram of mass, measured in Joules per kilogram or Grays.[4] Currently, several methods are used to quantify the absorbed dose such as calorimetry; ionisation chambers; semiconductors; and radiochromic films. While these detectors are adequate for current clinical radiotherapy, they are found to be insufficient for newer high dose or high dose rate treatment techniques. As stated in the following brief descriptions of these methods, each dosimeter functions in different ways and has both advantages and disadvantages.

The most direct method of measuring radiation energy deposited is through the use of a calorimeter[3]. Calorimeters measure the temperature rise as a result of energy absorption in a medium, usually water or graphite. These are usually conducted in a large insulated and

shielded container holding the absorbing medium. As radiation energy is imparted to the medium, it is ultimately converted into heat causing the temperature in the medium to rise. The temperature difference is measured with an external thermistor and the dose calculated from the known specific heat for that medium. However, this method is not practical in a clinical environment due to the large amount of radiation energy needed to increase the temperature for measurement by the thermistors and the lack of information about the spatial distribution of the dose[5].

One of the more common dosimeters in practice is the ionisation chamber. Ionisation chambers are gas filled cavities between two electrodes. Charged particles liberated by radiation are collected by the electrodes generating a current. The current flow is measured and converted into absorbed dose according to previous calibration. However, due to the non-tissue equivalent material of the detector, corrections must be made applied in order to determine the true absorbed dose. Another factor which impacts ionisation chamber accuracy is that the sensitive volume is susceptible to atmospheric conditions[3].

Semiconductor dosimeters include silicon diodes and metal-oxide semiconductor field effect transistor (MOSFETs). Radiation induces electron-hole pairs in the semi-conductor material and diffuses into the depletion region, generating a current. MOSFETs are transistor dosimeters that are based on measuring the threshold voltage. Radiation generates charges in the metal oxide layer, thus changing the threshold voltage in the MOSFET. Both the silicon diode and the MOSFET are only used as relative dosimeters, as they require dose calibration curves in order to convert either the current or the threshold voltage into absorbed dose. They must be calibrated regularly as the calibration changes over time[6].

Radiochromic films are self developing films that are almost tissue equivalent. The film contains a dye that polymerises and changes colour when exposed to radiation. As the polymer absorbs light, a densitometer can be used to measure the amount of light that passes through the film after exposure to determine the amount radiation it has absorbed. Disadvantage of radiochromic films are that it requires a non-linear calibration curve in order to relate it to the absorbed dose and the readout is not instantaneous[3].

1.2 Microbeam Radiation Therapy

Radiation therapy continues to evolve as new technologies are being developed and used. Microbeam radiation therapy (MRT) is an example of an advanced experimental technique, using radiation produced at a synchrotron facility is required. The beam is composed of an

array of parallel, microscopically thin slices of keV x-rays generated by the synchrotron. The beams are therefore modulated with peaks on the order of 20μm in width with an on-centre spacing of 200μm between the beams[7]. MRT has the capability to deliver these spatially modulated beams at very high doses and high dose rates (~1000Gy/s) in a fraction of the treatment time of conventional radiotherapy. The biggest advantage of MRT is the extraordinary tissue sparing effect of the micro beams, which is related to the so-called peak-to-valley dose ratio (PVDR)[8]. It was discovered that in MRT treatments, normal tissues have a high tolerance to an entrance dose of hundreds of Grays while cancerous cells are killed preferentially. This property makes it an ideal tool for superficial treatments and paediatric intracranial tumours while minimising collateral tissue damage[8]. However, the exact mechanisms for killing the cancerous cells are not well understood. One hypothesis is that uninjured normal cells undergo hyperplasia (increased cell division) and migrate from the regions in between the beams to replace the injured cells in the path of the beams[9].

Due to the nature of the micro beams (small spatial resolution, high dose gradient and polyenergetic), it is difficult to profile the beam or measure the PVDR. Several conventional dosimetric techniques exist and attempts have been made to adapt them to characterise MRT. Monte Carlo simulations formed the basis of many dosimetric efforts in predicting the profile and dose calculations, but lacked the validation of actual experimental dosimetry[10]. Other methods have also been tested; one study used the highly sensitive thermoluminescence response of Ge-doped silica optical fibres[11]. It offered reasonable spatial resolution (~125μm) and was able to characterise total dose in a MRT beam over a wide range of dose rates, however the energy response of the detector was unable to be devised and it was ineffective at measuring the PVDR. Another method utilising radiochromic films was tested to measure the dose profile[12]. Parallel sheets of films of different sensitivities were used where high sensitivity sheets would be used for the valley doses while low sensitivity sheets were used for peak doses. The films undergo darkening when exposed to radiation energy, however the darkening may not always be linearly correlated with the dose deposited and required further analysis in order to convert the optical densities into doses.

1.3 Research outline

As stated, current dosimetric methods have limitations for MRT mainly because of the physical dimensions and the non-tissue equivalence. As a result correction factors are required, as well as regular calibrations. Also discussed above is that previous dosimetric efforts to characterise MRT have not been able to satisfactorily resolve both the beam profile and the total dose delivered by the beam.

The idea in this work is to use the phantom medium itself as a sensor, in which the dose is read by an optical approach with sufficient resolution for MRT purposes. This method ensures minimal interaction with the radiation beam and the medium. The approach is quasi-calorimetric in nature and is based on one fundamental principle: the energy imparted by the radiation beam is ultimately converted into heat in the medium and as the temperature increases, the optical properties of the water also change - effectively a change in the refractive index. If the relationship between the temperature and refractive index is known then the absolute change in refractive index can be related to the temperature change, hence the radiation dose delivered into the phantom. To achieve this, the initial and final refractive index information must be recorded and recovered in order to find the difference.

1.4 Holographic Interferometry

Holography was invented in mid-twentieth century to provide a means to capture information about an object on photographic plates in the form of interference between wave fields scattered from the object and the reference wave. It was not widely used until recently when laser technology made longer coherence length lasers more economical. Further advances in holography techniques, such as holographic interferometry, allows the user to take 'snapshots' of an object's state in time, and permits comparison between the stored wavefronts within the holograms. This was especially useful in capturing how an object's refractive index has changed before and after applying an external force or process[13]. The refractive index change due to radiation can be measured through interferometry by passing a laser beam through the irradiated medium and combining it with a reference arm to form an interference pattern to determine the change in the optical path length of the laser beam due to the change in refractive index of the sample[14].

Hussman first demonstrated that holographic interferometry can be used to measure radiation energy deposited in a medium in 1971[15]. He used a low cost set-up, similar to a Michelson interferometer, in which the hologram was recorded on a holographic plate. The reconstructed interferogram was then used to calculate the dose profile within the medium. Other works[16, 17] also showed that interferometry and holographic interferometry, respectively, was able to measure the dose in terms of number of fringe shifts due to the change in the refractive index before and after irradiation. However, mobility and portability is limited in these setups due to difficulties in taking the setup outside of the laboratory environment for testing in clinical situations.

With the recent progress of digital detectors and computer processing power, holography is no longer restricted to bulky photographic plates. Digital detectors such as charged-coupled devices (CCD) replace photographic plates as the preferred option. Increased computer processing power allows rapid digital reconstruction of the object image based on the Fourier transform algorithm[18]. One of the biggest advantages of digitisation and reconstruction via Fourier transform is the ability to extract the phase information and compare with the reference state directly. However, one of the concerns of using digital detectors, especially CCDs, is that the photosensitive layer can be affected and sometimes permanently damaged by the presence of high energy x-ray radiation[19]. The radiation deposits energy within the oxide layer and liberates free electrons, forming voltage drift and false signals[20]. In order to avoid exposure to radiation, the detector needs to be sufficiently shielded, either by distance or physically. This led to suggestions of determining the viability of using a waveguide, such as optical fibres, to direct the signal out of the path of the radiation.

1.5 Thesis Outline

This research explores the possibilities of developing an optical fibre setup for dosimetric purposes and its viability as a proof-of-principle approach. Chapter 2 covers the theory and mathematics behind this method, from Maxwell's wave equation through to the conversion to dose. In chapter 3, the reconstruction of digital holography will be discussed. Chapter 4 details the practical considerations of optical experimentations specific to this setup, such as choice of laser used and methods of avoiding image overlap. Chapter 5 describes the development stages with different setups built and experiments performed. This is followed by the results of these experiments in chapter 6. The final chapter includes a summary and conclusion.

2. Background and Theory

In this chapter, the fundamental basis of the theories behind holographic interferometery is discussed, from Maxwell's wave equation through to the formation of holographic interferometry and the conversion of energy into radiation dose.

2.1 Overview of Approach

As mentioned in the previous chapter, the goal of this project is to construct a device capable of measuring radiation doses in a clinical setting. Interferometetry, more specifically digital holography interferometry, is a technique of hologram recording where the distorted wavefront through a sample is recorded to mathematically reconstruct a representation of the sample. The radiation dose measurement is based on calorimetry, where the radiation beam imparts energy into a transparent sample, typically a container of water. The energy is converted into heat and results in a raise in temperature. The elevated temperature in the water sample causes a change in its temperature-dependent refractive index. This change causes the optical path length through the sample to decrease and therefore a change in phase of a wave passing through it. When recorded in the form of holograms, the phase information can be extracted to theoretically calculate the energy that was imparted to the water.

This technique is based on interferometry; how an object light wave passing through a medium of interest interferes with a reference beam and diffraction theory; how light behaves when encountering an object, and how these will be measured. Fundamentally, the theory starts with the description of light propagation and light interference through to the Fresnel-Kirchhoff diffraction theory and how the object light wave is extracted from the interferogram; and how instances of the object light wave can be used to determine the refractive index change.

2.2 Interferometry

2.2.1 Principles of Interferometry

When two beams of light of equal frequency interact, a set of fringes, or alternating bright and dark bands appear, similar to figure 2.1. This phenomenon is called interference. The fringes contain information that would be otherwise unobtainable, such as the information about the wavefront and the phase difference of the two combined beams.

Figure 2.1: Observed fringe pattern of alternating bright and dark bands.

To observe interference, a simple Michelson Interferometer can be used to split a single light source into two beams and combine again to form an interference pattern at the screen, as seen in figure 2.2. The interference records the wavefront and the phase difference of the two beam paths: the unaltered path – the reference beam; and the path altered by the object - the sample beam. The overall phase change therefore can be attributed to the sample presence. If a sample, such as a water filled cuvette, is placed in the path of the object beam, we can extract the phase of the resulting wavefront from the interference pattern. A radiation beam can be applied perpendicularly to the water sample and thus altering the optical refractive index and thus changing the observed phase in the interference pattern.

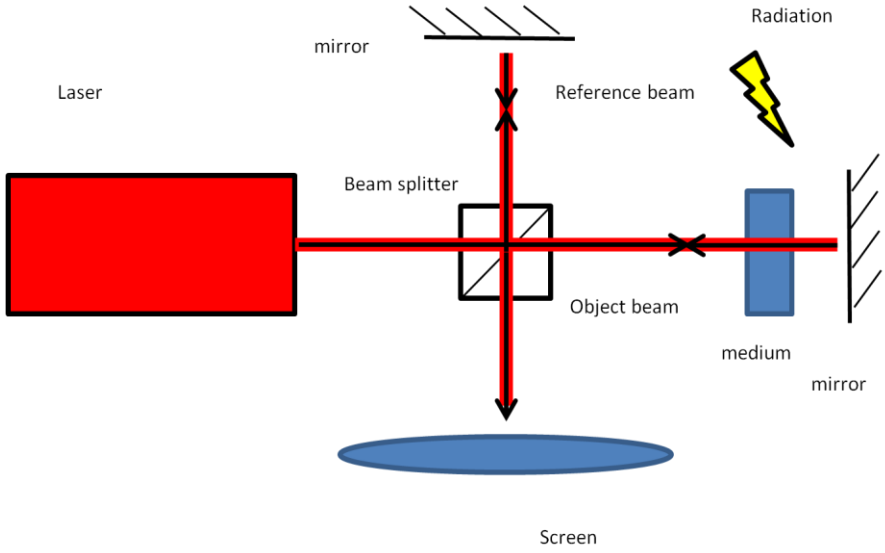

Figure 2.2: Michelson Interferometer.

2.2.2 Mathematics of Interferometry

Consider light propagation in a wave model, as described by Maxwell's equation[18, 21] in a vacuum:

$$\nabla^2\vec{E} = \frac{1}{c^2}\frac{\partial^2 E}{\partial t^2} = 0 \qquad (2.1)$$

A solution to the Maxwell's equation is an equation for a harmonic plane wave with electric field vector described by:

$$E(x,y,z,t) = a\cos(\omega t - \vec{k}\vec{r} - \varphi_0) \qquad (2.2)$$

Given a spatial vector $\vec{r}$ at time *t* propagating along $\vec{k}$ with amplitude *a;* a phase ofφ_0 , and its rotational frequency of ω. It can also be written in complex form:

$$E(x,y,z,t) = aRe[e^{\left(i(\omega t - \vec{k}\vec{r} - \varphi_0)\right)}] \tag{2.3}$$

Or simply taking the real part to represent the physical wave:

$$E(x,y,z,t) = ae^{\left(i(\omega t - \vec{k}\vec{r} - \varphi_0)\right)} \tag{2.4}$$

However, in most cases, only the spatial amplitude distribution part of the wave is considered:

$$E(x,y,z,t) = ae^{(i(\varphi_0))} \tag{2.5}$$

To describe the phenomenon of interference, consider two monochromatic waves with the same wavelength and polarization. Their complex amplitudes are:

$$A_1(x,y,z,t) = a_1 e^{(i(\varphi_1))} \tag{2.6}$$

$$A_2(x,y,z,t) = a_2 e^{(i(\varphi_2))} \tag{2.7}$$

The combined intensity of the two waves is:

$$\begin{aligned} I &= |A_1 + A_2|^2 \\ &= (A_1 + A_2)(A_1 + A_2)^* \\ &= {a_1}^2 + {a_2}^2 + 2a_1 a_2 \cos(\varphi_1 - \varphi_2) \\ &= I_1 + I_2 + 2\sqrt{I_1 I_2}\cos\Delta\varphi \end{aligned} \tag{2.8}$$

With I_1 and I_2 being the individual intensities of each wave and $\Delta\varphi = \varphi_1 - \varphi_2$. Equation 2.8 represents the sum of the individual intensities plus the sinusoidal varying term, or the interference term. This term is maximum, also known as constructive interference, when

$$\Delta\varphi = 2n\pi \quad for\ n = 0,1,2,\ldots \tag{2.9}$$

It is minimum or destructive interference when

$$\Delta\varphi = (2n+1)\pi \quad for\ n = 0,1,2,\ldots \tag{2.10}$$

Where *n* represents the order of the interference fringe, and depends on the phase or path length difference between the two beams. Hence this gives rise to alternating bright and dark bands called fringes as a result.

2.3 Digital Holography

In the case of holography, one wave A_1 represents the object wave E_O while A_2 represents the reference wave E_R. When recording a hologram, an object is placed in the path of the sample arm of the interferometer. As the light wave of the object beam hits an object, one would expect to find its outline of its shadow formed behind the object. However, if the size of the structure of the object is comparable to the wavelength then the outline of the shadow is not sharply defined, but a pattern of dark and light regions. This is called diffraction and is described by Huygen's principle[22]: *Every point on a propagating wavefront serves as the source of spherical secondary wavelets, such that the wavefront at some later time is the envelope of these wavelets.* This can be quantitatively shown by the Fresnel-Kirchhoff integral while considering the coordinate system shown in figure 2.3:

$$\Gamma(\xi',\eta') = \frac{i}{\lambda}\int_{-\infty}^{\infty}\int_{-\infty}^{\infty} A_1(x,y)\frac{\exp\left(-i\frac{2\pi}{\lambda}\rho'\right)}{\rho'}Q\,dx\,dy \tag{2.11}$$

Where

$$\rho' = \sqrt{(x-\xi')^2 + (y-\eta')^2 + d^2} \tag{2.12}$$

And

$$Q = \frac{1}{2}(cos\theta + cos\theta') \tag{2.13}$$

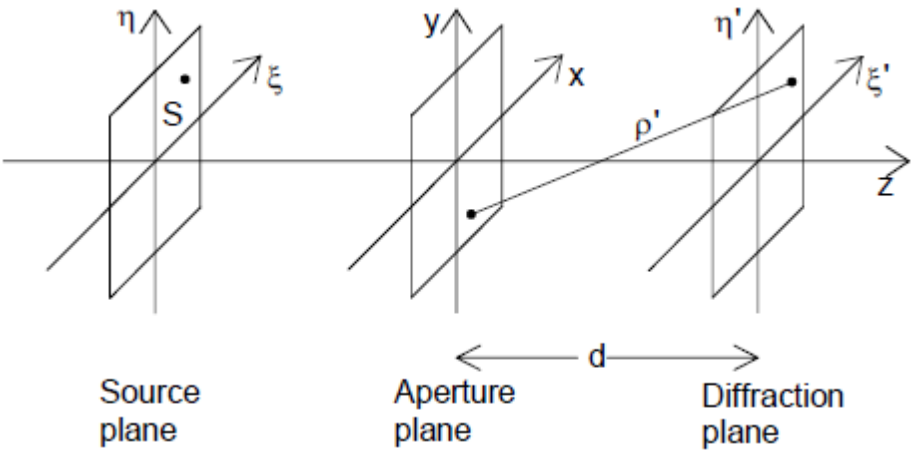

Figure 2.3: The coordinate system used in derivation of holography. In physical terms, the source plane represents the light wave and how it travels through an aperture in the aperture plane through to the diffraction plane where diffraction phenomenon of the wave can be observed[18].

Equation 2.11 considers a light source in the source plane with coordinates (ξ,η) radiating spherical waves outwards, and $A_1(x,y)$ is the complex amplitude of the wave in the aperture

plane. If an opaque aperture is considered with position (x, y) then secondary wavelets are emitted from this hole. The field $\Gamma(\xi', \eta')$ at the diffraction plane with position (ξ', η') is proportional to the incoming field from the aperture plane with complex amplitude $A_1(x, y)$ and to the secondary spherical wavelets emerging from it, described by $\frac{\exp(-i\frac{2\pi}{\lambda}\rho')}{\rho'}$. Where ρ' is the distance between a point in the aperture plane and a point in the observation plane, as described by equation 2.12. If the whole aperture plane is taken as many sources of secondary waves, then the field in the diffraction plane is simply the integral over all secondary waves from the aperture plane.

According to Huygen's principle, it is possible for secondary waves to propagate in the backwards direction. To eliminate this unphysical property, a Q factor must be introduced, as defined in equation 2.13. The Q factor depends on the angles θ and θ', the angle between the incident ray and vector perpendicular to the aperture plane; and the angle between the bended ray and the vector perpendicular to the aperture plane, respectively. However, the angles θ and θ' are approximately 0, the factor Q becomes 1 and can be neglected.

In the case of a numerical reconstruction the following coordinate system is defined in figure 2.4:

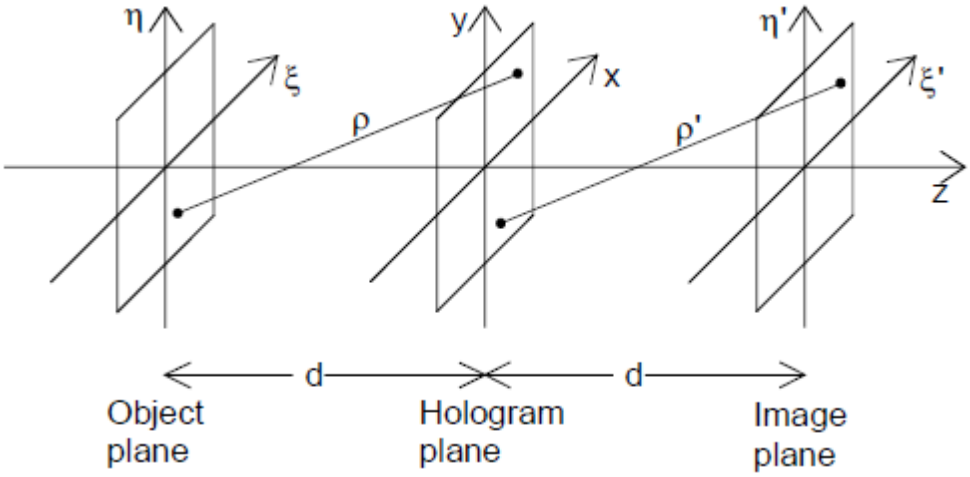

Figure 2.4: Coordinate system used in holography. The object plane represents the location in space of the object through to the formation of a hologram in the hologram plane and its reconstruction in the image plane[18].

Since $A_1(x, y)$ is the complex amplitude of the wave in the aperture, it equates to $h(x, y)$, the hologram function describing the beam passing though the object. It is proportional to the intensity of the interferogram recorded on the detector and when combined with the reference wave, or multiplied by the complex conjugate plane reference wave ${E_R}^*(x, y)$ in order to reconstruct the real image:

$$\Gamma(\xi,\eta) = \frac{i}{\lambda}\int_{-\infty}^{\infty}\int_{-\infty}^{\infty} h(x,y)E_R{}^*(x,y)\frac{\exp\left(-i\frac{2\pi}{\lambda}\rho\right)}{\rho}dxdy \tag{2.14}$$

Where

$$\rho = \sqrt{(x-\xi)^2 + (y-\eta)^2 + d^2} \tag{2.15}$$

This can be expanded by the Taylor series:

$$\rho = d + \frac{(\xi-x)^2}{2d} + \frac{(\eta-x)^2}{2d} - \frac{1}{8}\frac{[(\xi-x)^2+(\eta-x)^2]^2}{d^3} + \cdots \tag{2.16}$$

Where the fourth term is small compared to the wavelength and can be neglected:

$$\frac{1}{8}\frac{[(\xi-x)^2+(\eta-x)^2]^2}{d^3} \ll \lambda$$

Using this approximation and replacing the denominator in 2.14 by d:

$$\Gamma(\xi,\eta) = \frac{i}{\lambda d}\exp\left(-i\frac{2\pi}{\lambda}d\right)\int_{-\infty}^{\infty}\int_{-\infty}^{\infty} h(x,y)E_R{}^*(x,y)\exp\left[-i\frac{\pi}{\lambda d}((\xi-x)^2+(\eta-y)^2)\right]dxdy \tag{2.17}$$

With further expansion of the integral:

$$\Gamma(\xi,\eta) = \frac{i}{\lambda d}\exp\left(-i\frac{2\pi}{\lambda}d\right)\exp\left[-i\frac{\pi}{\lambda d}(\xi^2+\eta^2)\right]\int_{-\infty}^{\infty}\int_{-\infty}^{\infty} h(x,y)E_R{}^*(x,y)\exp\left[-i\frac{\pi}{\lambda d}(x^2+y^2)\right]\exp\left[i\frac{\pi}{\lambda d}(x\xi+y\eta)\right]dxdy \tag{2.18}$$

To digitize the equation, the following substitutions are made:

$$\nu = \frac{\xi}{\lambda d};\ \mu = \frac{\eta}{\lambda d} \tag{2.19}$$

2.18 becomes

$$\Gamma(\nu,\mu) = \frac{i}{\lambda d}\exp\left(-i\frac{2\pi}{\lambda}d\right)\exp[-i\pi\lambda d(\nu^2 + \mu^2)]\int_{-\infty}^{\infty}\int_{-\infty}^{\infty} h(x,y)E_R{}^*(x,y)\exp\left[-i\frac{\pi}{\lambda d}(x^2 + y^2)\right]\exp[i2\pi(x\nu + y\mu)]\,dxdy \tag{2.20}$$

Assuming the hologram function *h(x, y)* is sampled on a CCD detector with N x N pixels with Δx and Δy as pixel sizes in horizontal and vertical directions, respectively. The integrals in 2.20 become discrete finite sums:

$$\Gamma(m,n) = \frac{i}{\lambda d}\exp\left(-i\frac{2\pi}{\lambda}d\right)\exp[-i\pi\lambda d(m^2\Delta\nu^2 + \eta^2\Delta\mu^2)]\sum_{k=0}^{N-1}\sum_{l=0}^{N-1} h(k,l)E_R{}^*(k,l)\exp\left[-i\frac{\pi}{\lambda d}(k^2\Delta x^2 + l^2\Delta y^2)\right]\exp[i\pi 2(k\Delta x m\Delta\nu + l\Delta y n\Delta\mu)] \tag{2.21}$$

To relate the different planes according to the Fourier theory, the following substitutions are made:

$$\Delta\nu = \frac{1}{N\Delta x};\ \Delta\nu = \frac{1}{N\Delta y} \tag{2.22}$$

And

$$\Delta\xi = \frac{\lambda d}{N\Delta x};\ \Delta\eta = \frac{\lambda d}{N\Delta y} \tag{2.23}$$

Then 2.21 become:

$$\Gamma(m,n) = \frac{i}{\lambda d}\exp\left(-i\frac{2\pi}{\lambda}d\right)\exp\left[-i\pi\lambda d\left(\frac{m^2}{N^2\Delta x^2} + \frac{n^2}{N^2\Delta y^2}\right)\right]\sum_{k=0}^{N-1}\sum_{l=0}^{N-1} h(k,l)E_R{}^*(k,l)\exp\left[-i\frac{\pi}{\lambda d}(k^2\Delta x^2 + l^2\Delta y^2)\right]\exp\left[i\pi 2\left(\frac{km}{N} + \frac{ln}{N}\right)\right] \tag{2.24}$$

Equation 2.24 allows the finite sums to be approximated by the inverse two dimensional Fourier Transform.

If the reference wave is a point source, a spherical wave in the plane of the object can be described by:

$$E_R = \frac{\exp\left(-i\frac{2\pi}{\lambda}\sqrt{(d^2+x^2+y^2)}\right)}{\sqrt{(d^2+x^2+y^2)}} \approx \frac{1}{d}\exp\left(-i\frac{2\pi}{\lambda}d\right)\exp\left(-i\frac{\pi}{\lambda d}(x^2+y^2)\right) \tag{2.25}$$

The Fresnel Transform simply becomes:

$$\Gamma(\xi,\eta) = const\exp\left[-i\frac{\pi}{\lambda d}(\xi^2+\eta^2)\right]\Im^{-1}\,h(x,y) \tag{2.26}$$

with the phase:

$$\varphi(k,l) = arctan\frac{Im[\Gamma(\xi,\eta)]}{Re[\Gamma(\xi,\eta)]} \tag{2.27}$$

And the interference phase difference between two snapshots of the object is simply:

$$\Delta\varphi = \begin{cases} \varphi_1 - \varphi_2, & if\ \varphi_1 \geq \varphi_2 \\ \varphi_1 - \varphi_2 + 2\pi, & if\ \varphi_1 < \varphi_2 \end{cases} \tag{2.28}$$

However, due to phase differences being measured in 2π modulo, it must first be unwrapped to obtain continuous phase information. This will be discussed in chapter 3.

2.4 Conversion into Temperature and Energy

The phase shift obtained represents the change in the optical path length (OPL) the laser beam has travelled. Since the phase is measured in the number of two pi shifts, it must be converted into number of wavelength shifts and the wavelength to find the physical change in the OPL:

$$\Delta OPL = \frac{\Delta\varphi}{2\pi}\lambda \tag{2.29}$$

Since

$$OPL = nd \tag{2.30}$$

Where *n* is the refractive index and *d* is the physical length then:

$$\Delta OPL = \Delta nd \tag{2.31}$$

So:

$$\Delta nd = \frac{\Delta\varphi}{2\pi}\lambda \tag{2.32}$$

With $\Delta n = n_2 - n_1$, the refractive index difference between two instances of the object, where n_1 is the initial refractive index, and n_2 is the final refractive index i.e. after a change in temperature.

Refractive index changes with temperature, but the relationship is not clear and it can only be determined experimentally. Several works [23-26] were reviewed to find the best fitted model in terms of its standard error, and the model chosen was by Dobbins et al with refractive indices correct to 6 decimal places. The initial refractive index can be calculated from the Dobbins et al.'s formula below, assuming the experimentally determined refractive index of 1.332156 for He-Ne light (632.8nm) at 20 degrees Celsius in standard conditions:

$$dn(T)\text{x}10^5 = -8.889(T-20) - 0.1610(T-20)^2 \tag{2.33}$$

The above formula states the change of refractive index from the fixed point at 20 degrees Celsius. It also states that refractive index decreases as temperature increases between 20 and 30 degrees Celsius, hence decreasing optical path length. We can assume all the radiation energy imparted in the medium is converted to heat as the energy used for intrinsic reactions within the medium can be negligible[15]. Once the final temperature of the sample is calculated from the refractive index change; the temperature change is used in the calorimetry equation to determine the energy absorbed[27]:

$$E = c_p m \Delta T \tag{2.34}$$

Where E is the energy, c_p is the specific heat capacity for water, m is the mass of the water and ΔT is the change in temperature of the water sample. Since radiation is typically measured in Grays (Gy), with equivalent units of joules of energy absorbed per kilogram of mass then:

$$D = \frac{E}{m} = c_p \Delta T \tag{2.35}$$

2.5 Concluding remarks

This chapter described the formation of interference patterns through the fundamental Maxwell's equation for waves and how it diffracts around an object allowing us to reconstruct the object wave. Furthermore, the digitization and the subsequent treatment with the two-dimensional inverse Fourier Transform allowed simple reconstruction and extraction of phase information. The phase information was in turn related the dose imparted in the sample. In the next chapter, the process of measuring dose with holographic interferometry through the extraction of temperature information from the recorded phase differences is described.

3. Reconstruction

In this chapter, we will discuss the digital image reconstruction aspect of the holography. This will include the treatment of raw recorded holograms in MATLAB; as well as methods to improve the recorded image; and theories behind phase unwrapping.

3.1 Image Reconstruction

In order to obtain meaningful data, the recorded holograms need to be processed to reconstruct the image representations of the original object. According to the theory in described in chapter 2, the Fresnel–Kirchhoff Integral can be used to reconstruct these images. It can be approximated by equation 2.26 in digital terms as:

$$\Gamma(\xi,\eta) = const \exp\left[-i\frac{\pi}{\lambda d}(\xi^2+\eta^2)\right]\Im^{-1}\,h(x,y) \tag{2.26}$$

The important part of the equation is $\Im^{-1}h(x,y)$ where it is the inverse Fourier transform of the recorded hologram function (or image); and the other terms are simply constants. The Java-based computer program MATLAB was used for fast processing of original holograms into image representations of the object. A code script (attached as appendix) was written to automate this process for a series of images in order to compare between instances of the object state.

The images are recorded in the compressed format of 'JPEG', or 'TIFF', a non-compressed format. The latter is preferred but due to size considerations, the former was used sometimes. The holograms are recorded in three colour (red, green and blue) layers, and since only intensity is required for image reconstruction, the layers are combined. However, the first (red) colour layer can be solely used as the green and blue layers mostly comprise of intensity values of 0 due to the dominant colour from a red He-Ne laser. An example of a hologram recorded using a modified Michelson Interferometer setup is shown in figure 3.1.

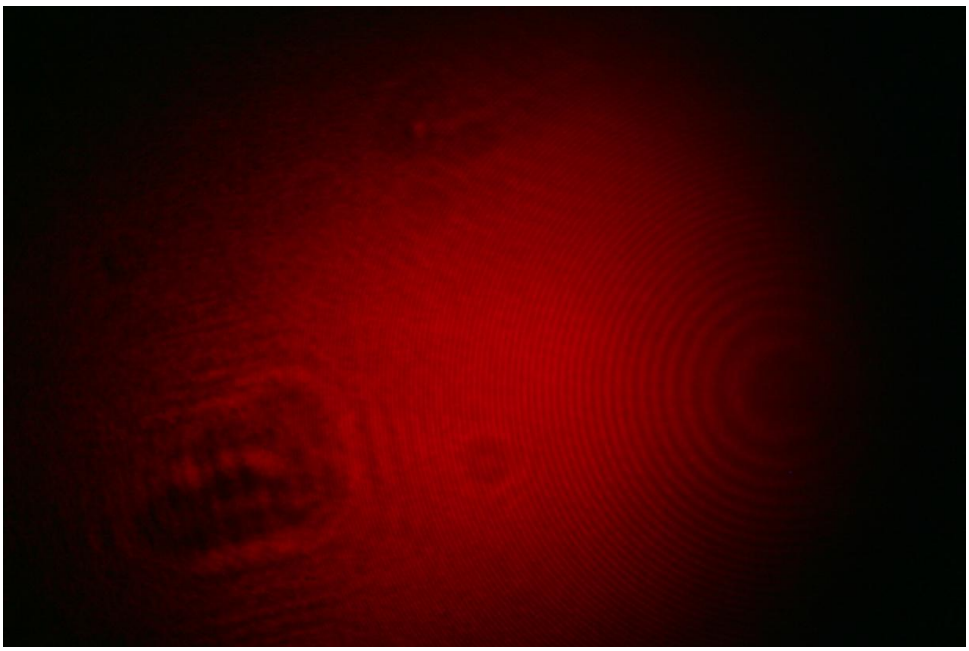

Figure 3.1: A recorded hologram of a printed letter 'F' on an overhead transparency, blurred by the diffraction pattern around its edges. This hologram showed the dominant red colour from the He-Ne laser light.

The built-in inverse Fourier transform MATLAB function ('ifft') is used, as denoted by equation 2.26, to reconstruct the hologram into an image representation of the object. However, the opposing quadrants in the image must be swapped due to the discrepancy in the coordinate systems between MATLAB and equation 2.26. MATLAB assumes top left corner to be the origin (0, 0 in Cartesian) whereas the equation assumes the centre to be the origin. The resultant image is an array of complex numbers and the logarithmic of the absolute reconstructed intensity displayed in figure 3.2. However, the reconstructed image shows the real image on the right, its virtual twin image on the left, and the central bright DC term. A zoomed in display of the real image can be seen in figure 3.3.

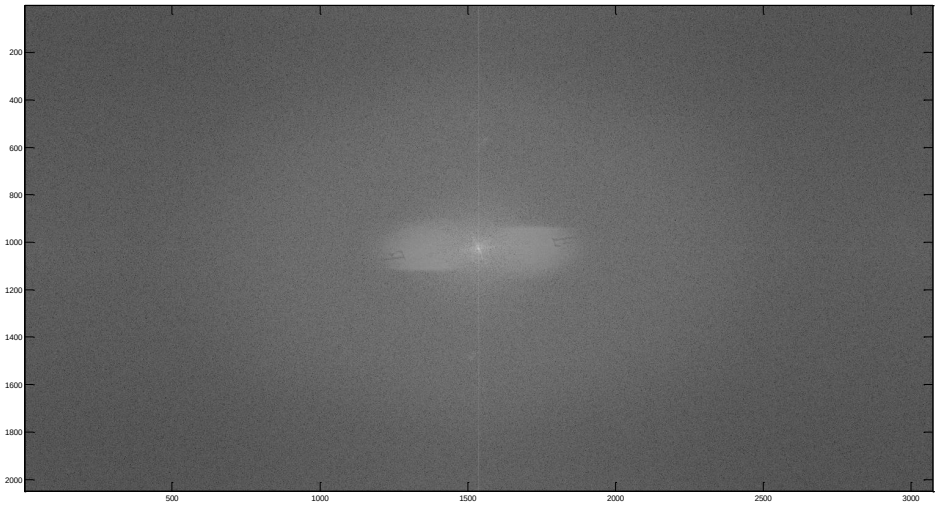

Figure 3.2: Reconstructed image of the previous hologram, clearly showing the letter 'F'. The axes denote pixels.

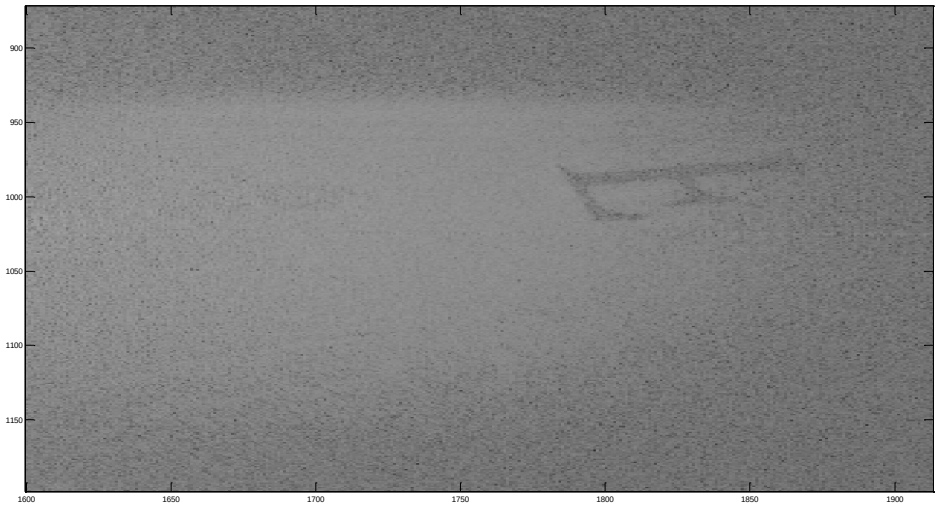

Figure 3.3: Reconstructed image of the hologram in figure3.1 and zoomed in on the real image of 'F'.

One of the problems encountered in the reconstruction was the superposition of the image with the central bright DC term. An example of this can be seen in figure 3.4 below. The DC term covers part of both the real image and its virtual twin.

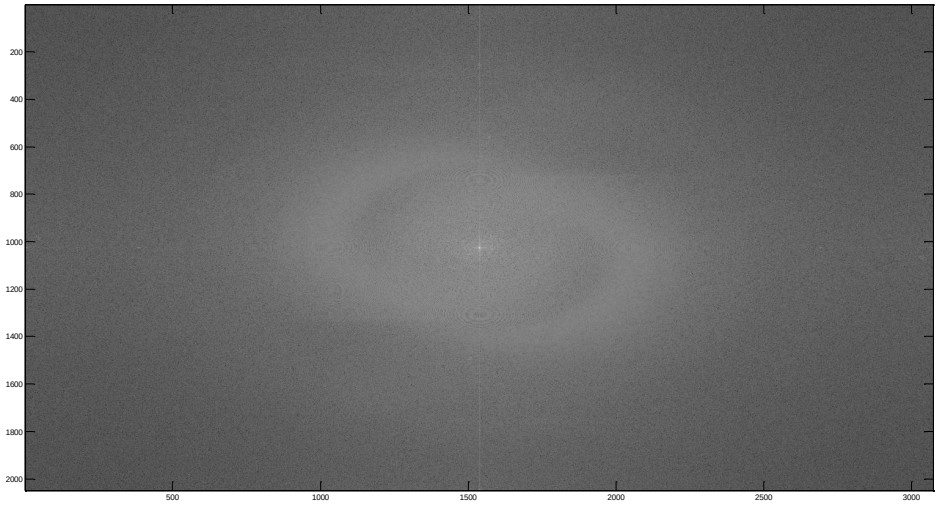

Figure 3.4: An example of a reconstructed image showing DC term overlaps with the real and virtual images.

There are two solutions to this problem; first using DC suppression techniques which require post processing methods; the other solution is to make a small adjustment to the setup to avoid the overlap. So far, the mathematics in chapter 2 described the original inline holograms and its approximate reconstruction via the Fourier transform. The adjustment needed was to introduce a small angle between the reference beam and the object beam to offset the superposition in the image plane, a technique called off-axis holography[28, 29]. It was first used by Leith and Upatnieks[30] in 1962 to take advantage of the first coherent laser

source. They showed that by giving the object and reference beams different directions and made to overlap in the hologram plane to induce interference, the reconstructed wavefronts were spatially separated in the imaging plane. The orientation of the beams is better explained in figure 3.5 below. However, this imposes another requirement in the setup and the detector resolution to counteract this change due to the spatial frequency sampling needs. This will affect the choice of detector used in the setup and will be explained in detail in the next chapter.

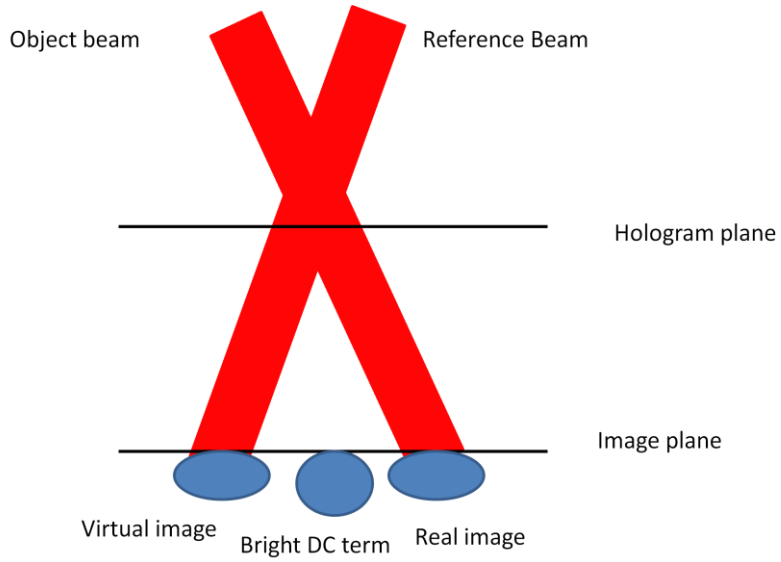

Figure 3.5: To avoid superimposed images and the DC term, an angle is introduced between the reference and object beams so that they overlap in the hologram plane.

3.2 Phase Unwrapping

After an image has been reconstructed, only the phase information is of interest and is required to find the refractive index. MATLAB can calculate the phase information with a simple command and display it accordingly. However, phase is an angular property of a continuous wave and calculated from the complex function. As a consequence, it can only be recognised to within $\pm\pi$ radians or modulo 2π radians. If the phases are supposedly continuous then seemingly random phase jumps appear, this problem is known as wrapped phase. This can be better explained using a continuous function such as in figure 3.6[31]. The figure shows the case of a one-dimensional phase function to jump up to a value of almost 3 then suddenly dropping back down to -3. Given that the expected underlying phase is actually continuous and not spiking up and down as shown in the figure, then the values for the phases are incorrect.

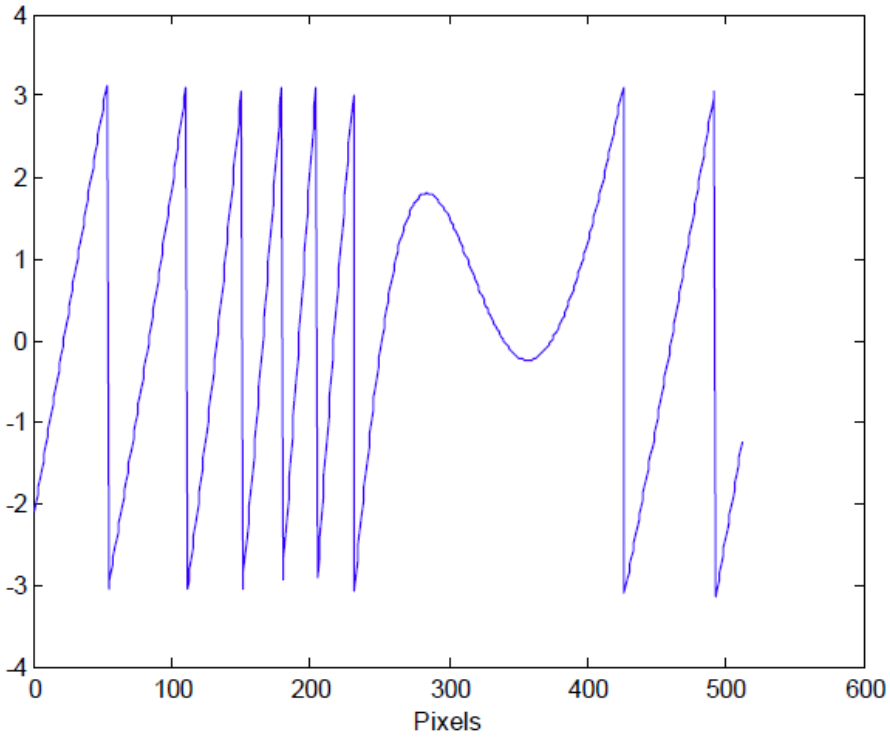

Figure 3.6: Generated continuous one-dimensional phase function with its phase jumps, or wrapped phases[31].

One solution to this problem is to simply compare the current phase value with its previous neighbour in order to determine its true phase. But this technique requires an accurate starting phase in order to find the next phase in relation to it. MATLAB has a built in command for this and can easily unwrap one-dimensional functions, and the result of the unwrapping can be seen in figure 3.7. As clearly shown, the phase information is a smooth curve, without the peaks and valleys in figure 3.6.

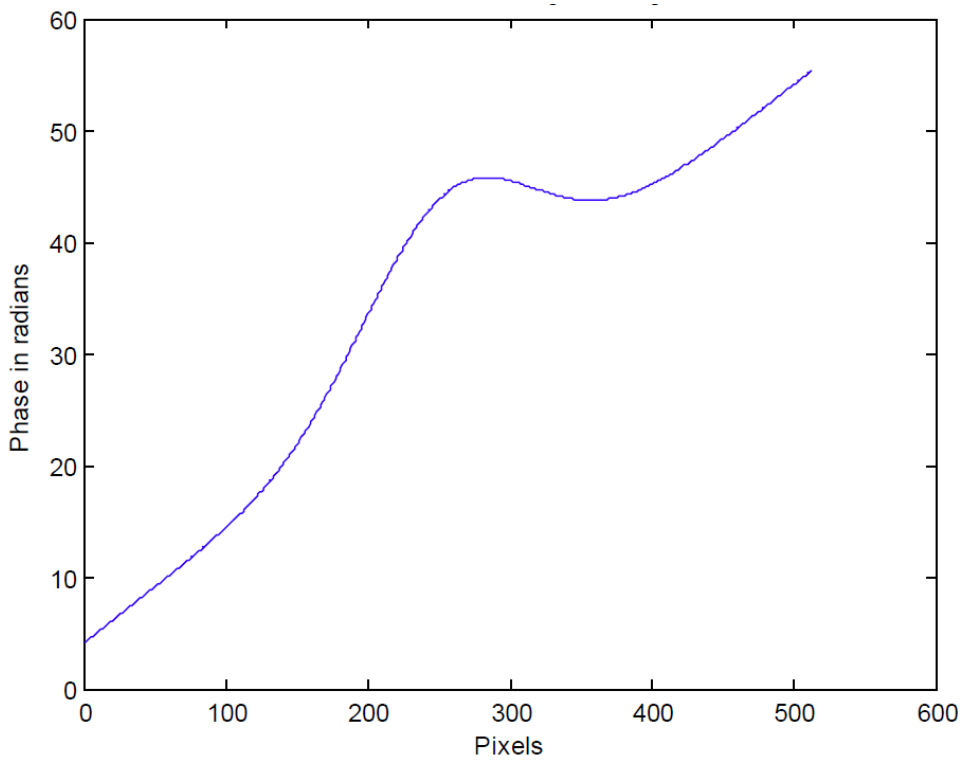

Figure 3.7: Unwrapped phases of a continuous wave from figure 3.6 [31].

However, unwrapping phases is not as simple in two-dimensional or even three-dimensional cases as the above one dimensional example. Often, in two-dimensional images, the continuous phases do not run in easily recognisable patterns and an accurate starting point is not immediately identified. Added to this, in real experimental data sets, there is often unaccounted noise which can have a huge impact on the outcome of the unwrapping[32]. Methods have been devised to unwrap phase information by utilising stable starting points and to follow paths set by line integrals; and others by evaluating and comparing the residues in order to reduce noise and improve accuracy in the image.

The unwrapper used in the implemented reconstruction was the Herráez et al.[33] two-dimensional phase unwrapping algorithm. It is one of the methods that calculate the reliability of each pixel from a pre-determined reliability function. Then the reliability is assessed to establish edges in order to find a starting point and subsequently a path for unwrapping. Multiple edges can be found and hence multiple paths are followed, resulting in groups of unwrapped pixels. The groups are then compared by the number of pixels and their reliability values in order to determine how the groups are compared into one and this process is repeated until the entire image becomes one group of pixels. Although this algorithm is complex, it is relatively quick and was chosen mainly for its speed and simplicity in its MATLAB implementation in the form of a C script that was compiled in MATLAB by means of the 'mex' function.

Since the experiment is about comparing instances of the refractive index change of a sample over time, it may become necessary to unwrap the phases in the time dimension. A three-dimensional phase unwrapper may be employed for this purpose but the expected phase changes over time should be very small. Considering that a phase difference of 2π equates to approximately 3000Gy in radiation dose at room temperature, the three-dimensional phase unwrapper may prove redundant.

3.3 Concluding remarks

In this chapter, we have discussed the digital image reconstruction aspect and treatment in MATLAB; as well as the wrapped phase problem and the implementation of a phase unwrapper to counteract it. The equations for reconstruction and 2D phase unwrapping were implemented in MATLAB. In the next chapter the actual physical step is discussed.

4. Setup Requirements

So far, we have discussed the mathematics and theory, as well as the digital reconstruction, in this chapter we will describe some of the requirements a practical setup needs. There are several equipment factors that must be taken into consideration for an optical setup. Firstly, the coherence length of the laser used; secondly the type of laser used and lastly the detector type and the angle required between the reference and object beams.

4.1 Laser type

There are many types of lasers available for experimental research purposes, but some has features that are more advantageous over others, depending on situation. In this setup, the laser used was a Helium-Neon (He-Ne) laser and was chosen for a variety of advantages over others. Since the laser beam is expected to pass through the sample, its interactions with the sample must be considered. Most significant of these effects is the absorption of the laser light by the sample. Ideally, the laser used should completely pass through the sample and minimise energy loss to the sample. If the sample absorbs too much energy then it would induce heating effects and thus affecting the accuracy of the experiments for dosimetry. He-Ne lasers emit at a wavelength of 632.8nm, red light in the visible range. As shown in figure 4.1, the absorption of water is minimal in the red visible range and hence minimal energy is transferred into the sample causing heating effects. Other advantages of He-Ne are its relatively stable output beam and its long coherence length.

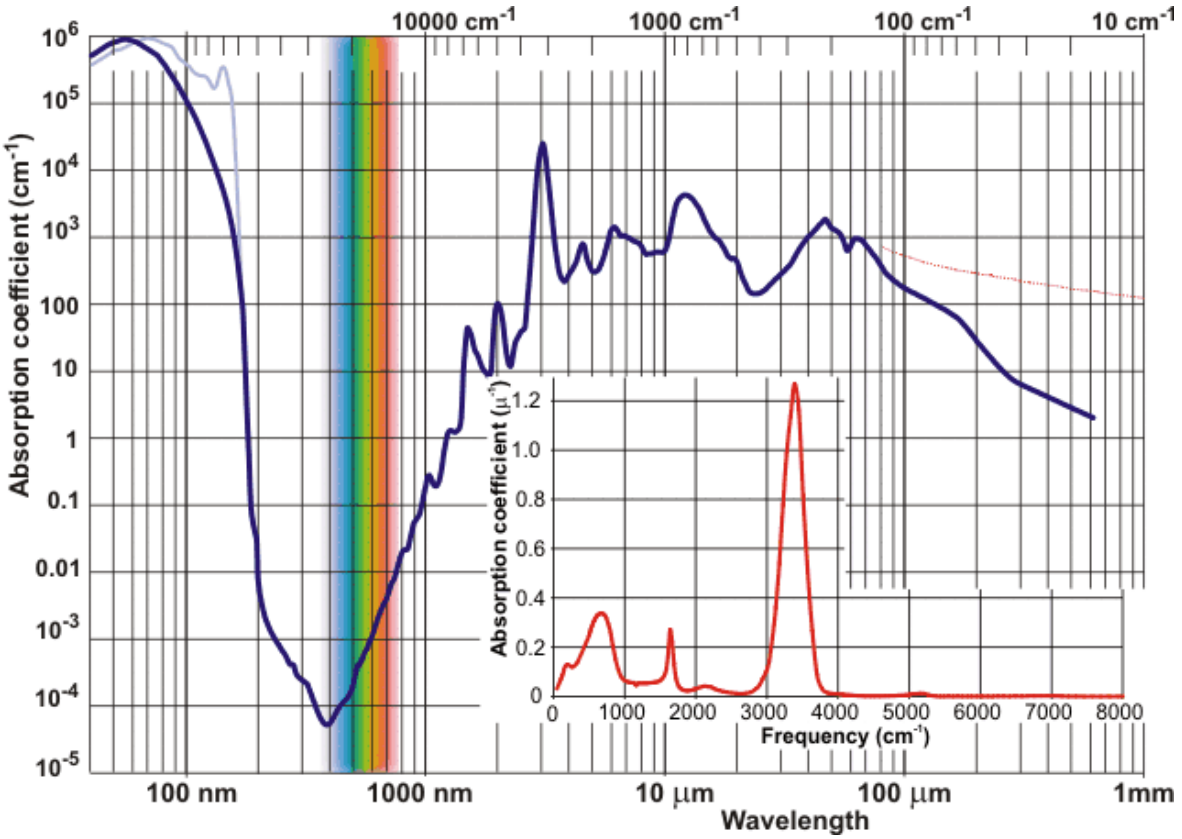

Figure 4.1: Absorption of various wavelengths of light in water[34].

However, He-Ne lasers are not without disadvantages. One of the drawbacks of He-Ne laser is the long lasing tube and its bulky power supply unit. While this is not an issue in the laboratory where the setup is fixed, it may be an issue when transportability is taken into account. For this reason, semiconductor diode lasers in the red 660nm visible range were also considered. The diode laser was the size of a pen laser pointer and the lasing unit could easily be incorporated into the setup. It had much higher power output than the He-Ne, rated at 100 milliwatts compared to 10 milliwatts on the He-Ne. The diode draws low level of current and can be powered by batteries, which potentially could be substituted with power from a computer USB port.

4.2 Laser coherence

In interferometry, two beams combine to generate the alternating dark and bright fringes. However, to produce the fringes required, the laser and the setup must fulfil some conditions. This property is called coherence, it describes how the two beams are correlated with each other and is essentially limited by the light source, in this case, the Helium-Neon laser. There are two types of coherence: spatial and temporal. Spatial coherence describes the instance where two geometrically different parts of the same wavefront combines to generate

interference. Essentially, this case only applies to wavefront division techniques; it is of little consideration in this setup.

We will focus here on temporal coherence that describes how a wave correlates with itself at different instances of time. Physically in a continuous wave, this represents the distance between random disturbances. The temporal coherence length of a laser can be found by using a Michelson interferometer, as shown in figure 4.2. The beam from the laser, in this case a red He-Ne laser, is split into two at the beam splitter, with one beam passing through and the other reflected at ninety degrees. Both beams are reflected back by the mirrors in their paths towards the beam splitter again and combine on the screen. An interference pattern is observed if the path length of the two beams is smaller than the coherence length. But, as the movable mirror is adjusted, the path length between the two beams changes and as the distance increases, the interference can no longer be observed. The maximum path length difference between the two beams allowed for observable interference is called the coherence length. In the case of this particular He-Ne laser, the coherence length was determined to be approximately 15cm using the method outlined above. Repeating the experiment for the diode laser, it was found to be approximately 8cm.

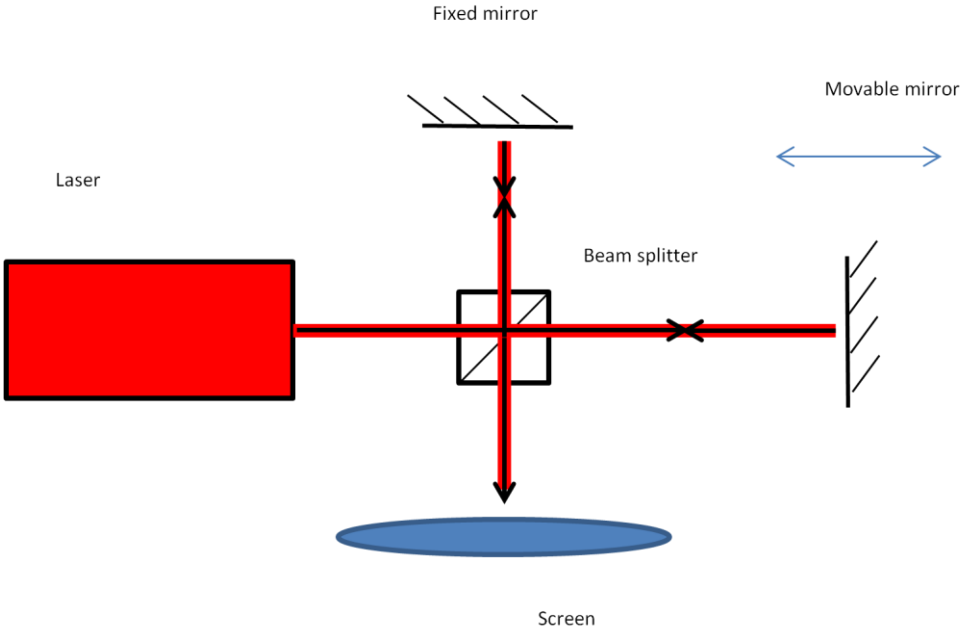

Figure 4.2: Schematic of a Michelson Interferometer setup used to determine the coherence length of a laser.

4.3 Detector and sampling

The detector used to record images in most experiments is a charged-coupled device (CCD); it is an array of sensitive elements outputting digital signals and therefore has finite resolution and must fit the spatial frequency requirements. As mentioned briefly in the

previous chapter, the two beams must combine at an angle to avoid DC-term overlapping with the real and virtual images. Therefore, the detector places a restriction on the range of angles allowed and is governed by the interference pattern fringe spacing, i.e. the distance, d, between neighbouring maximums:

$$d = \frac{\lambda}{2\ sin\frac{\theta}{2}} \tag{4.1}$$

Where θ is the angle between the two beams.

According to sampling theory, the fringes, or simply period must be sampled with more than two pixels, in other words:

$$d\ > 2\Delta\xi \tag{4.2}$$

Where ξ is the size of a pixel on the detector (assuming pixels are square), then:

$$2\Delta\xi\ < \frac{\lambda}{2\ sin\frac{\theta}{2}} \tag{4.3}$$

If expressed in terms of spatial frequency $f = \frac{1}{d}$ and taking the small angle approximation taken into account then the angle requirement becomes:

$$\theta\ < \frac{\lambda}{2\Delta\xi} \tag{4.4}$$

The detector used in most experiments was a digital single lens reflex (DSLR) camera, with pixel resolution of 7.4 μm x 7.4μm. This equates to a maximum angle of approximately 2.4 degrees between the object and reference beams.

4.4 Experimental Setups

From the initial simple interferometer setup through to the fibre injection setup, we will describe in this section the apparatus and the reasons behind the designs.

4.4.1 First Setup

The first setup devised is depicted below in figure 4.3. The output beam from He-Ne laser was split using a non-polarising beam splitter into reference and sample beams. The sample beam passed straight through the beam splitter while the reference beam was reflected off a mirror and redirected towards the detector.

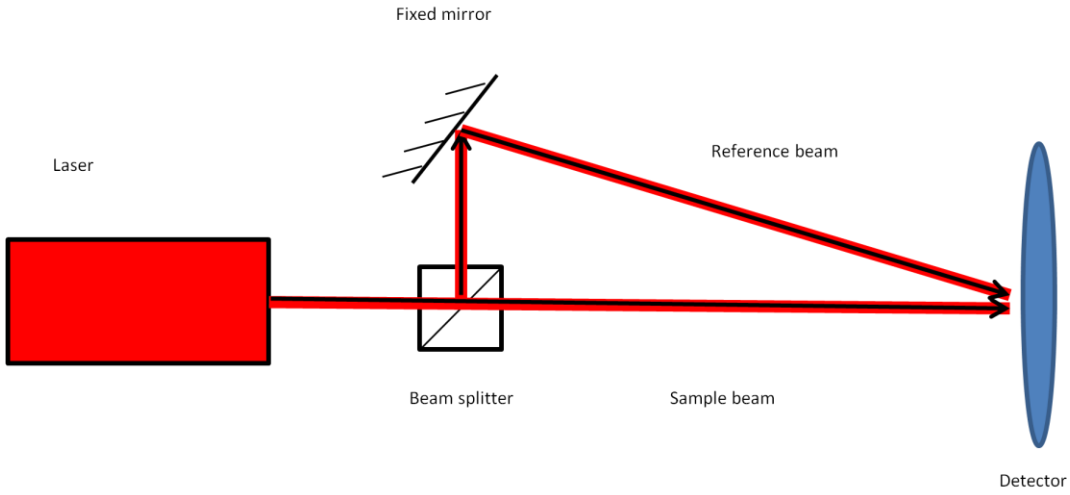

Figure 4.3: Schematic of the Initial setup of an interferometer. The beam was split by the beam splitter; the sample beam through the beam splitter while the reference beam diverted by the beam splitter at 90 degrees. The reference beam reflects off the mirror and recombines with the sample beam at the detector. The angle between the reference and sample beams is greater than 2.4 degrees at short distances and becomes impractical at longer distances.

However it was soon realised that this setup does not satisfy the coherence requirements, as described in the previous chapter. The reference beam travelled extra distance, greater than the coherence length, to reach the detector when compared to the sample beam and was limited by the minimum practical length between the beam splitter and the mirror. Recall the angle requirement imposed on the setup in order to spatially separate the DC-term and the real and virtual images from the previous chapter, this setup could fulfil it if the detector was sufficiently distant to minimise the angle. But in practice the distance needed was very large and impractical to do so. The initial detector was a simple webcam (JVC Dual-Mode Digital Camera GC-A33) with a detector resolution of 640x480 pixels. However, there was a lens in front of the detector that refracted the beams so the beams did not combine in an expected manner. To solve these problems a new setup was devised.

4.4.2 Second Setup

In order to create two paths that are almost identical in length (within coherence length of the laser), a second beam splitter was introduced to the setup, as depicted in figure 4.4, resembling a Mach-Zehnder interferometer. This second beam splitter acts to combine the beams to allow for interference to occur at the detector.

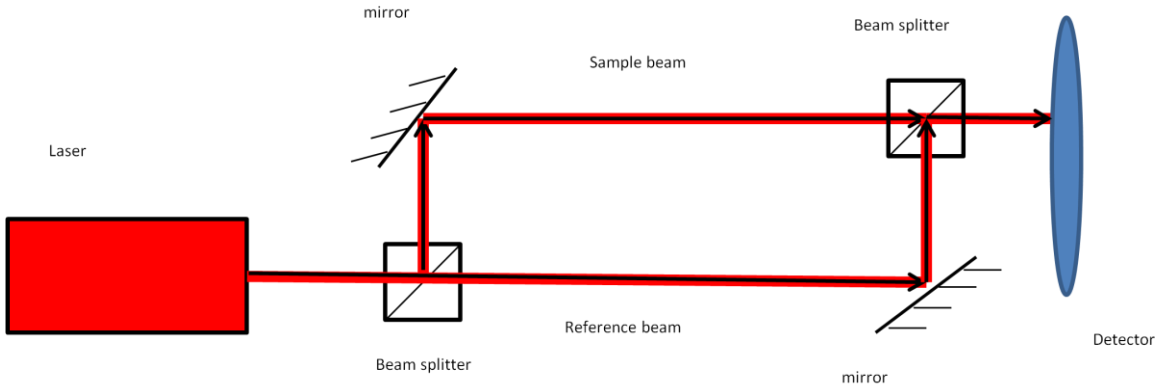

Figure 4.4: Schematic of modified setup from figure 4.3. As in the previous setup, a beam splitter splits the laser output into the sample and reference beams. The new addition is the inclusion of a second beam splitter to recombine the sample and reference beams.

4.4.3 Third Setup

To correct for the small angle problem, the sample beam was put in at a slight angle, with the second beam splitter would be slightly rotated off-axis as shown in figure 4.5 below. The sample beam would pass straight through the rotated beam splitter while the reference would be reflected at an angle to the normal.

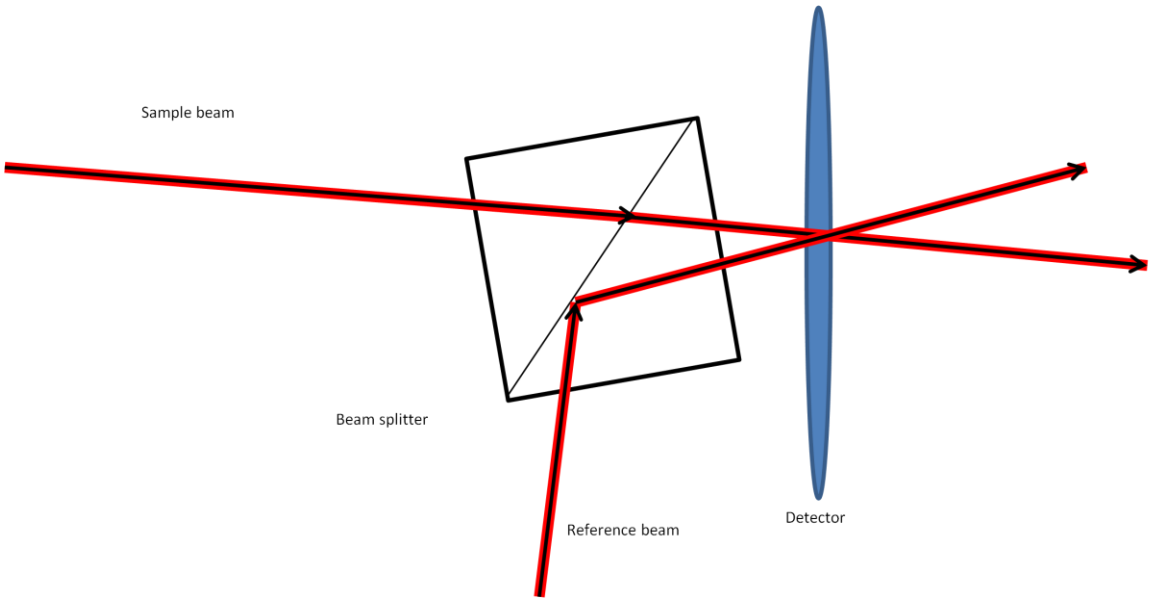

Figure 4.5: Detailed depiction of orientation of beam splitter and incoming beams. The reference beam is slightly off-axis when passing through the off-angle beam splitter; subsequently the reference beam reflects at an angle slightly larger than 90 degrees. The beams recombine at the detector.

Since the output beam from the laser has a small diameter (approximately 2mm), a telescope of two lenses (lenses 1 and 2 with focal lengths 16.5mm and 200mm respectively) was used in the sample beam path to enlarge it to a reasonable size of 2cm. The magnification ratio of the beam depends on the ratio of the focus distances of the lenses. Also as stated in the theory in chapter 2, a divergent reference beam is required in order to simplify the

reconstruction, hence another lens (lens 3 focal length of 16.5mm) was included in the reference beam for this purpose. The beam sizes were matched at the detector. With these inclusions, the new schematic can be seen in figure 4.6. A new detector was chosen, a digital single lens reflex (DSLR) camera (Canon EOS 300D)[35] with its lens unit removed so that the light falls directly onto the CCD detector. Since the new detector was very sensitive, neutral density filters of 1% and 0.1% were placed in front of the detector to reduce the incident light.

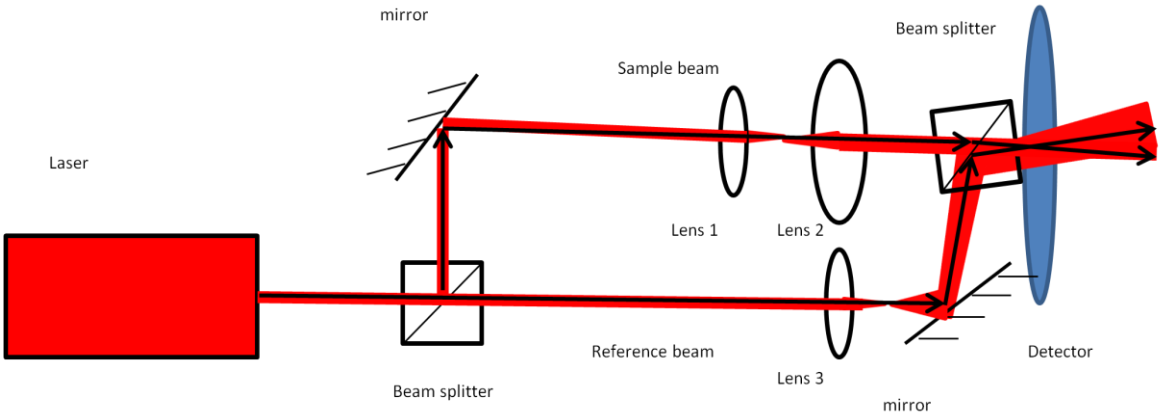

Figure 4.6: Modified setup from figure 4.4, incorporating a second beam splitter depicted in figure 4.5. Changes include the telescope of two lenses to expand the slightly off-axis sample beam; a small lens in the reference beam to create a divergent wavefront; and rotated beam splitter to compensate the small angle.

4.4.4 Fibre injection setup

The next evolution of the setup looked at replacing the sample and reference beams with waveguides. Waveguides such as optical fibres were considered to be incorporated because of concerns over possible radiation damage to electronic components such as the laser tube and to increase the transportability of the setup. Optical fibres act to guide laser light while the electronic components can be sufficiently shielded by distance.

The first challenge was to put light from the laser output into a piece of optical fibre. The core diameter of single mode fibre at 632nm was very narrow (4.3μm) and required precise optics in order to do this. A three axis micrometre-precision injection stage was used for this purpose where laser light output was focused with a short focal length lens into the optical fibre core. In the previous setup a beam splitter was used to divide the laser output into the reference and sample beams, in this instance, the beam splitter was replaced by a 50/50 fibre coupler (SM630 manufactured by OEMarket)[36]. The fibre outputs were cleaved and placed in bare-fibre connectors and clamped down to provide a stable output. Matching the beam orientation of the previous setup, the output beams passed through the unmodified part of

the setup. However, there were extra light losses at laser injection so the neutral density filters were changed accordingly. The new schematic can be seen in figure 4.7.

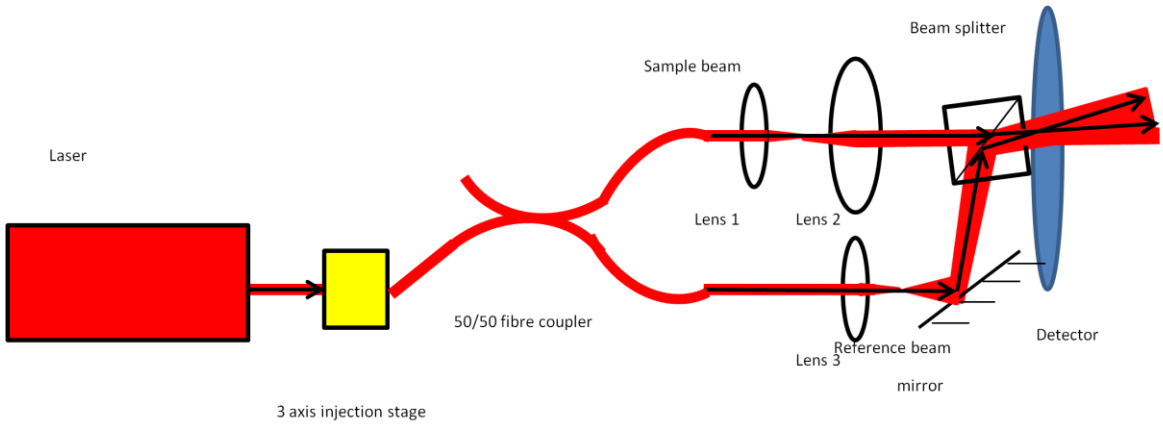

Figure 4.7: Schematic for fibre input setup. Light from the He-Ne laser was injected into a single mode optical fibre (at 633nm), passes through a 50/50 fibre coupler to split into two equal outputs to become the sample and reference beams.

4.4.5 Camera replacement

The next step was implementing a detection method through optical fibres that replaced the camera, as with the previous setup, the aim was to use waveguides to direct the light to detectors away from the potential radiation sources the sample might be exposed to. The detector considered in this case was a photodiode sensitive in the visible range, attached to the end of the output fibres. The photodiode is made from semiconductor material that converts incident light into voltages, hence a single photodiode can only 'read' a single point in the hologram at any given time. Therefore, a scanning method was required to feed the image 'point by point' to the photodiode.

To translate the image in space, a set of two perpendicular moving mirrors mounted on galvanometers (Cambridge Technology Model 6215H)[37], driven by precision drivers (Cambridge Technology MicroMax 671xx Single Axis)[38] was used for scanning. The mirrors rotate within a range in order to direct the image along an axis. The speed and range of the moving mirrors is determined by an external frequency generator. However, to ensure accuracy the moving galvanometer mirrors were designed to be very small in size; hence the reference and sample beams must be focused with another lens onto these mirrors. So in place of where the detector was in the previous setup, the new lens with short focal length was placed in order to focus the images onto the set galvanometer driven mirrors. The images were then scanned across bare end of an optical fibre mounted on an injection stage and fed to the photodiode detector (Thorlabs DET10A - Si Detector)[39]. A range of options can be used to record the data from the photodiode; one method was to link the photodiode to a data acquisition (DAQ) card (Measurement Computing USB1608-FS)[40] linked to a

computer to record the voltage values to build up the scanned image. The setup schematic can be seen in figure 4.8 below.

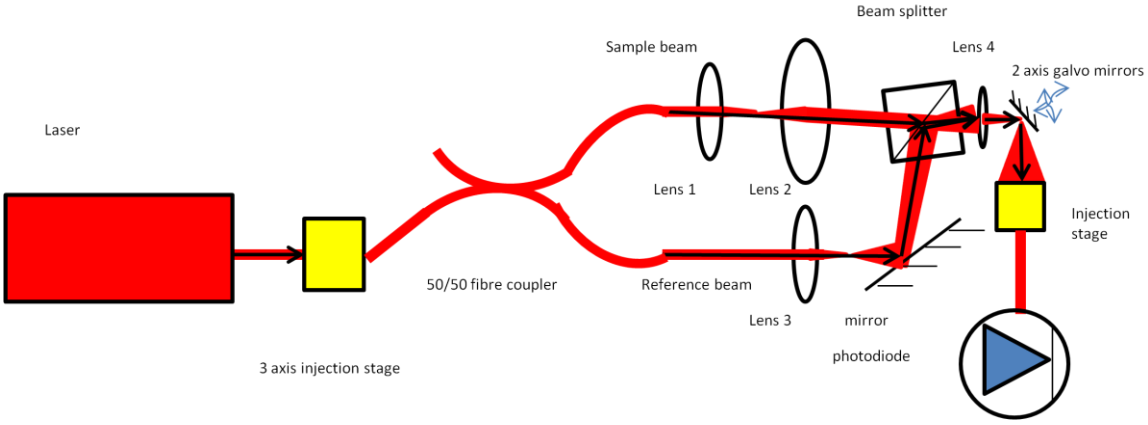

Figure 4.8: Schematic for new setup with photodiode detection. The image is scanned by a 2 axis galvanometer-driven mirrors and injected into an optical fibre for detection at the attached photodiode. The output voltage readings are recorded with a DAQ card on a computer as an array to represent the image.

4.5 Concluding Remarks

In this chapter, we have discussed the reasons behind the choice of laser and detector, as well as how the components were incorporated into various interferometer setups. In the next chapter, the experiments conducted with the setups are described.

5. Experiments

In this chapter we will describe the experiments conducted to test various aspects and responses of the setups devised.

5.1 Calibration

This test was designed to test the alignment and the angle of the beams. Letters were printed on an overhead transparency to act as samples. The transparency was placed in the path of the sample beam, so that the shadow of the chosen printed letter fell on the detector. The hologram was recorded and used to reconstruct the object. The separation and the angle of the beams were adjusted until a satisfactory separation was obtained. Other small objects with distinct outlines were also used for calibration, such as small resistors.

The second part of the test involved using a small transparent microscope slide. It was placed in the path of the sample beam, in a way so only a portion of the beam passes through the slide. This was designed to introduce a known constant phase change to part of the sample beam and to test the reconstruction algorithm in its ability to distinguish the phase difference.

5.2 Detector Saturation

The second test conducted was to determine the saturation of the detector. The detector used was a DLSR camera; hence there was a need to adjust it to find the optimal response in order to capture the images. A fixed sample of the letter 'D', printed on overhead transparency, was used to take a series of images to determine the best ISO speed and shutter speed in order to not saturate the detector and obtain pictures of the best quality for subsequent trials. The intensity distributions of the recorded holograms were used to establish the saturation of the pixels in the detector.

5.3 Phase Gradient

As mentioned in chapter 2, the refractive index and therefore phase is dependent on the temperature, so the next experiment focused on the phase response of the setup. As we expect a distribution of dose that varies with depth for radiation dosimetry, we wanted to mimic a similar phase gradient in this experiment. A gradient can be established by heating

water, inducing a change in phase through the beam that can be detected at the output of the interferometer. A standard spectrophotometer quartz cuvette filled with distilled water was suspended in the path of the sample beam. Being careful to not disturb the water, a small metal rod was used as a reference point as well as heat conductor. It was clamped in a way that part of it was submersed in the water, while a flame was heating the exposed end, as shown in figure 5.1 below.

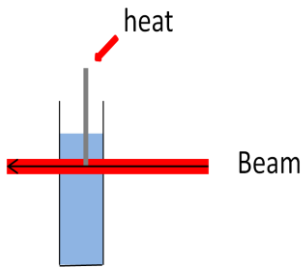

Figure 5.1: Placement of metal rod in relation to cuvette and beam. The rod was clamped above the cuvette with part of it in the water and the path of the sample beam to act as a reference point in the images. The exposed end of the rod was heated with an open flame and conducts it in the water.

5.4 Laser Heating

To imitate the heating effect of an x-ray radiation source, a powerful infrared (IR) laser (tuneable Raman Laser) was used as a means of applying electromagnetic radiation to a water sample. The IR laser was supplied via an optical fibre and mounted above the cuvette, pointing down into the water in the cuvette, as seen in figure 5.7. The laser was tuneable in terms of both wavelength and power. The wavelength was set at 1489nm and the power was varied in the experiments to determine the degree of heating required. Images were taken at intervals in order to determine the heating throughout the time period and presumed to be at steady state (i.e. the rate of heating equals the rate of heat dispersion) after 20 minutes. The reference image was taken initially before any heating, and the phase change calculated using equation 2.28.

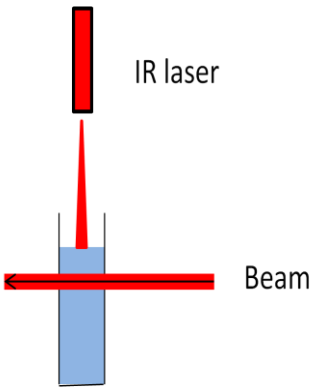

Figure 5.2: The IR laser was mounted IR laser above the water sample in cuvette, with its output pointed downwards into the water to induce heating.

5.5 Stability Tests

Due to very small expected temperature changes in dosimetric practices, the system needed to be tested on its stability and reliability. Without heating or adjusting the water sample, a series of images were taken in a quick burst to determine the stability of the system in a very short time frame. Another series of images were over a longer period of time at regular intervals to determine its long term stability. These images were then compared to the reference using equation 2.28 to determine how the sample phase has changed over time without any interference.

5.6 Concluding Remarks

The experiments conducted and the reasons behind the experiments for each setup were described. In the next chapter, the results of the experiments are discussed.

6. Results and Discussion

The results from the experiments (described in the previous chapter) from each setup will be presented in this chapter. Also, the implications of the results have on the setups will be discussed.

6.1 Initial Setups

6.1.1 Calibration

Initial efforts resulted in overlap of the real and virtual images with the bright DC term in the centre of the image plane, the initial hologram can be seen in figure 6.1a. The reconstructed image of the letter 'B', plotted in the logarithmic of the absolute intensity in figure 6.1b, showed that there was partial overlap in the real and virtual images with the central bright DC term, highlighted by the red boxes.

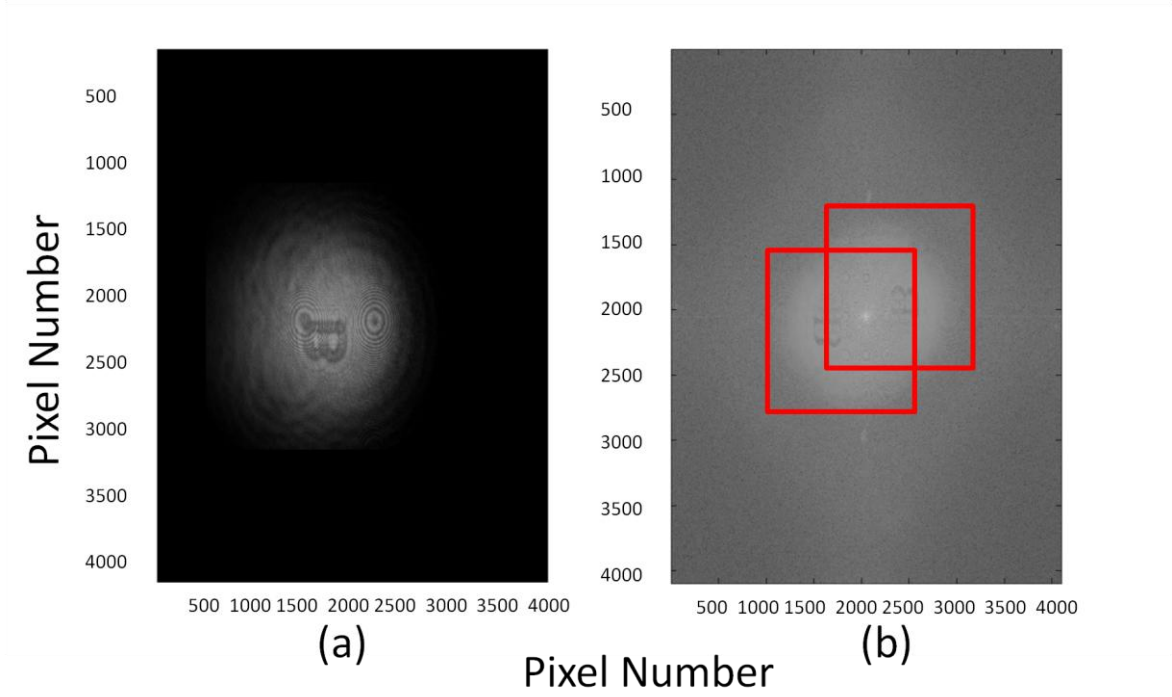

Figure 6.1 (a): The recorded hologram on the CCD detector. (b): Reconstructed image of the alphabet 'B', plotted in logarithmic of the absolute intensity, clearly showing the overlap of the images (overlapping red boxes) with the central DC term, resulting in a slight blurring of the 'B'.

As the angle in the first setup cannot be adjusted, modifications were needed to in order to tweak the angle. This problem was solved with the addition of a second beam splitter to recombine the beams, as detailed in section 4.4.3. The angle can then be adjusted by the

rotation of the recombining beam splitter and the incident angle of the reference beam. This process was repeated until the separation was acceptable. Figure 6.2 shows an example of sufficient separation in the imaging plane. The 'F' in the reconstructed image on the right can be clearly seen without overlap, as highlighted by the red boxes on figure 6.2b.

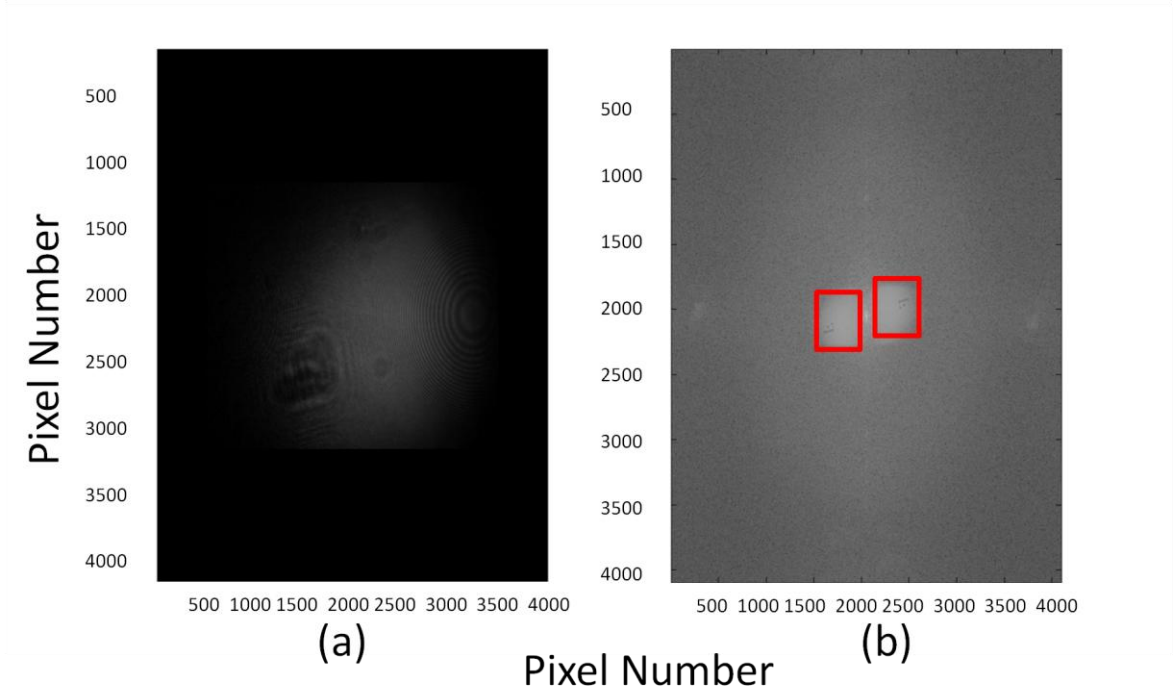

Figure 6.2: (a): Recorded hologram. (b): Reconstructed image of 'F'. In this example the angle was sufficiently large to separate the images in the imaging plane to avoid overlapping (highlighted by red boxes).

However, other noticeable effects were also experienced. One of these was 'copies' of the images appearing in the imaging plane, as shown in figure 6.3b. This effect can be traced to the optics equipment. Images of the object reflected off the surfaces of the beam splitters and/or lenses in the setup and into the detector and subsequently reconstructed in the image. This effect can be avoided by tilting beam splitters and lenses so that the beams passing through these were slightly off-axis, ensuring the multiple reflections do not reach the detector.

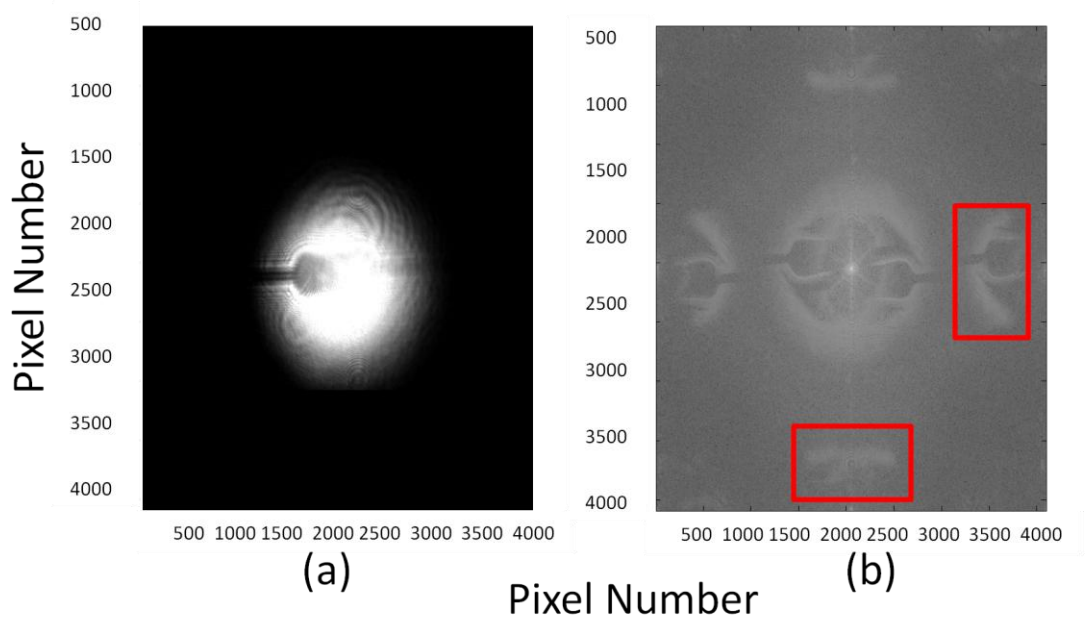

Figure 6.3: (a): Recorded hologram of a resistor. (b): Reconstructed image of a resistor and its mirror images (highlighted in red boxes), due to back-reflected images of the object from beam splitters and/or lenses.

6.1.2 Phase test

After establishing acceptable angular separation in the imaging plane, the next set of experiments designed to extract the phase information from the images. As mentioned in the theory in chapter 2, the phase information is the property of interest and it leads to the determination the refractive index changes and hence finding the temperature. A simple standard transparent glass microscope slide was placed in the lower part of the sample beam. The zoomed in and extracted pseudo-coloured phase diagram from the reconstructed image can be seen in figure 6.4. As shown, the lower part of the beam is uniform in phase, whereas the top part is a modulo 2π distribution since no unwrapper was applied. Outside of the circular beam, the speckle noise represents random noise where there was no illumination.

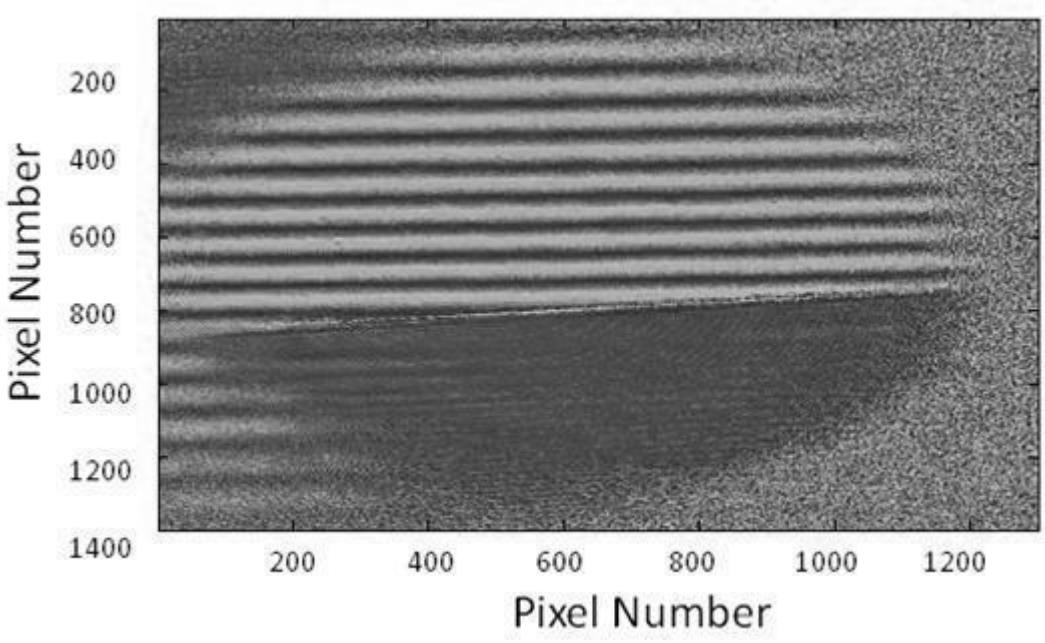

Figure 6.4: Extracted phase image from the reconstructed image of glass microscope slide. The glass slide covers the bottom half the beam, as shown by the uniform part of the diagram; while the top half of the beam shows the modulo 2π distribution phase.

6.2 Fibre injection setup

6.2.1 Calibration

As with the previous setup, initial holograms were made to determine the angular separation. One of these examples can be seen in figure 6.5. The reconstructed image of the letter 'D' on the right of figure 6.5 clearly shows the virtual and real images were well separated to avoid the bright DC term.

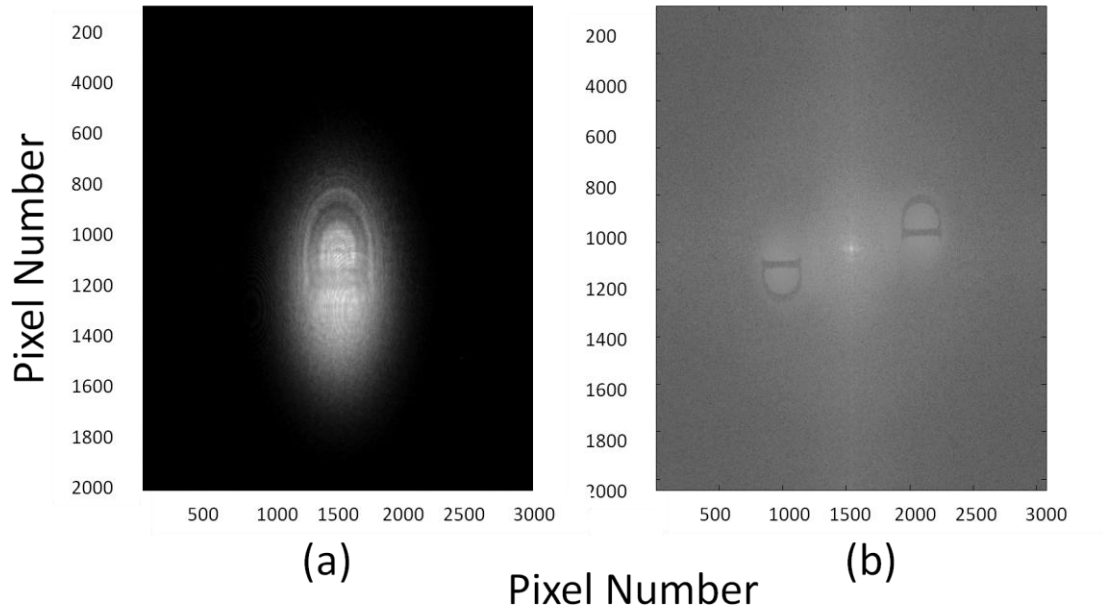

Figure 6.5: Test calibration hologram (a) and its reconstructed image (b) of 'D'. The virtual and real images can be clearly seen and spatially apart in the reconstructed image.

6.2.2 Detector Saturation

The detector used was a CCD; each pixel is assigned a numerical value between 0 and 255, inclusive, to denote the amount light incident on it. The amount of light allowed to hit the detector is dependent on the ISO speed, the sensitivity of the detector; and the shutter speed, the interval of time the shutter opens to allow light to fall onto the detector. A series of images were taken with varying shutter speed at two different fixed ISO speeds. The holograms were recorded as normal and then analysed with pixel intensity histogram counts. Figure 6.6 shows a sample of the holograms (left) made with 1600 ISO speed and their respective pixel intensity distribution (right). With a shutter speed of 1/1000s, the image is very faint while 1/250s was clear but the intensity distribution suggests that a large portion of the intensity values were not used. 1/50s and 1/10s showed a number of pixels with maximum intensity. This suggests that part of the detector was saturated in intensity.

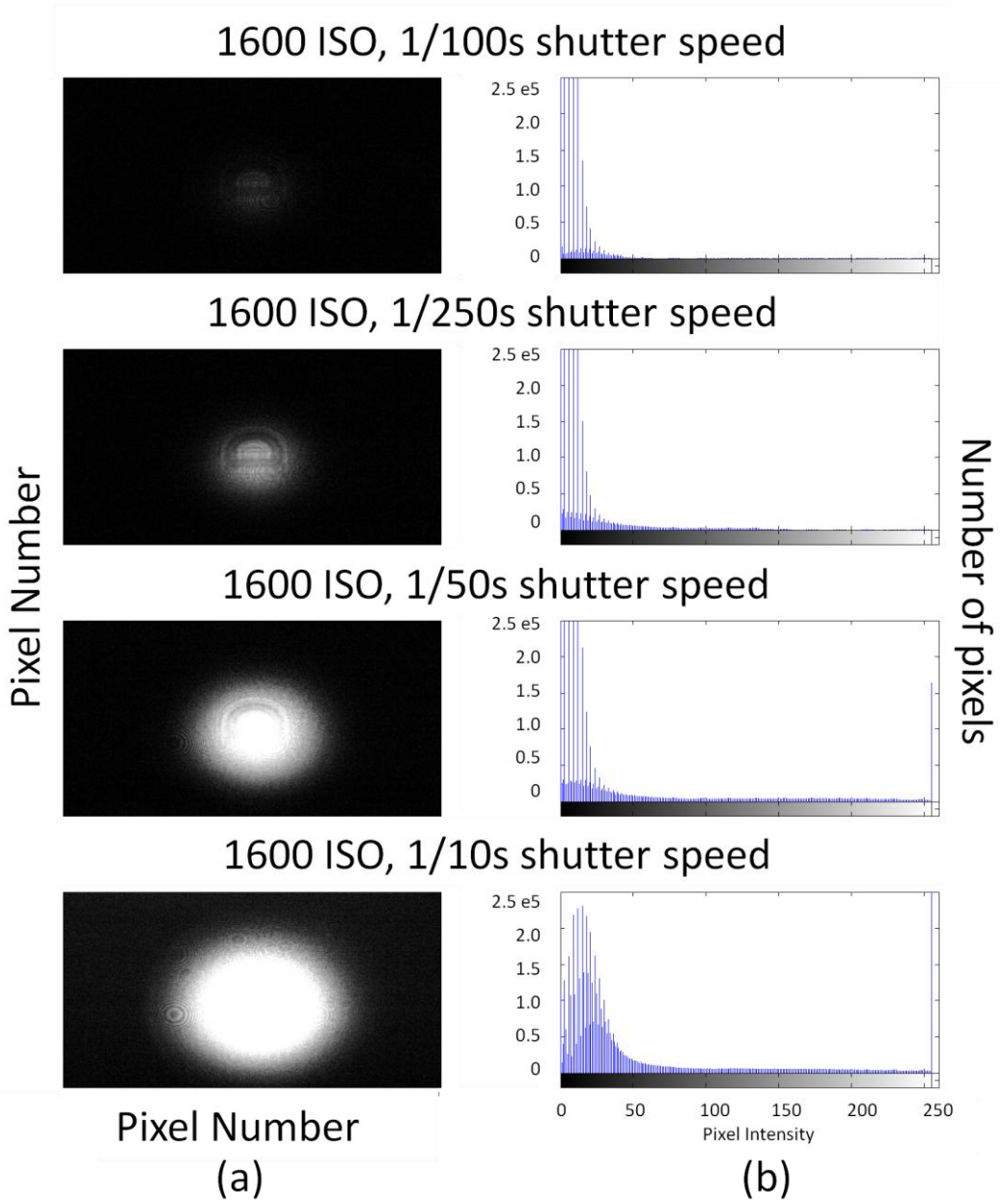

Figure 6.6: Holograms taken using the 1600 ISO speed and shutter speeds as labelled (in seconds). (a): the left column presents the recorded holograms; the right column (b) presents the histogram of the intensity distribution of pixels. Holograms taken with 1/100 and 1/250 are dimmer confirmed by their respective histograms to be unsaturated; whereas 1/50 and 1/10 holograms are much brighter and their histograms show they are indeed saturated.

Figure 6.7a shows a sample of the holograms made with 400 ISO speed and their respective pixel intensity distribution in figure 6.7b. With a shutter speed of 1/500s, the image is very faint while 1/150 was clear but the intensity distribution suggests that a large portion of the intensity values were not used. 1/25s distribution shows a number of pixels at the maximum intensity, while not significant; it still showed that there was saturation. 1/50s distribution showed that more than two thirds of the intensity distribution was used, hence this setting was chosen for subsequent pictures.

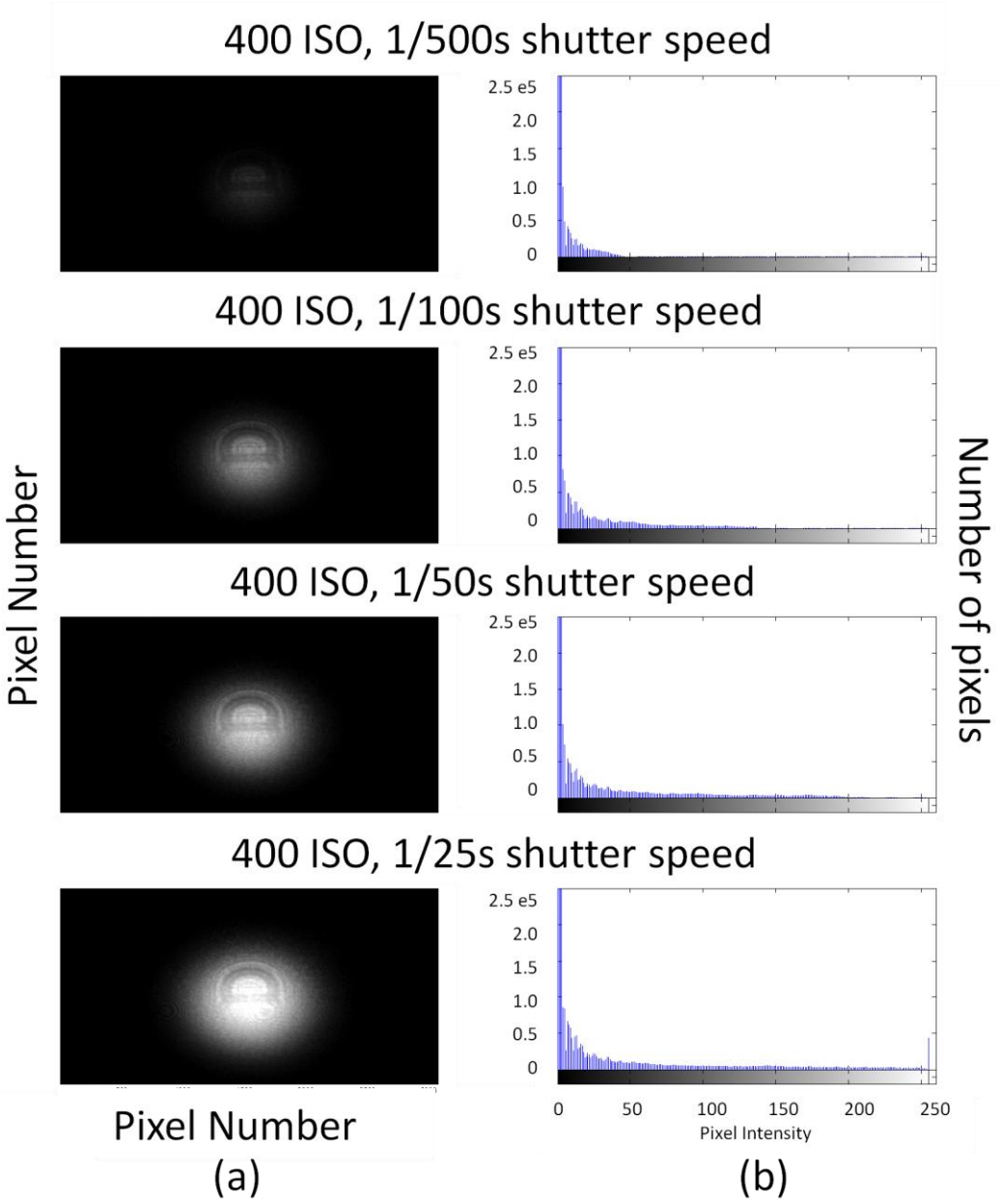

Figure 6.7: Holograms taken using the 400 ISO speed and shutter speeds as labelled (in seconds). (a): The left column presents the recorded holograms; the right column (b) presents the histogram of the intensity distribution of pixels. Hologram taken with 1/500 shutter speed is very dim, its histogram show the distribution biased towards the low intensity values. Hologram taken with 1/100 shutter speed is also dim; its histogram show the distribution skewed towards the low intensity values, less so than 1/500. The histogram of 1/50 show that some pixels are approaching the maximum intensity but none has that value. The histogram of 1/25 show that some pixels saturated at maximum intensity.

6.2.3 Water heating with metal rod

An initial hologram was taken without any heating applied to act as reference state, from which all changes in the subsequent holograms would be compared to. The captured hologram can be seen below in figure 6.8a and the reconstructed image can be seen on the

right in figure 6.8b, where the red box highlights the object. It shows that the image is upside down, as the rod was inserted from the top of the cuvette.

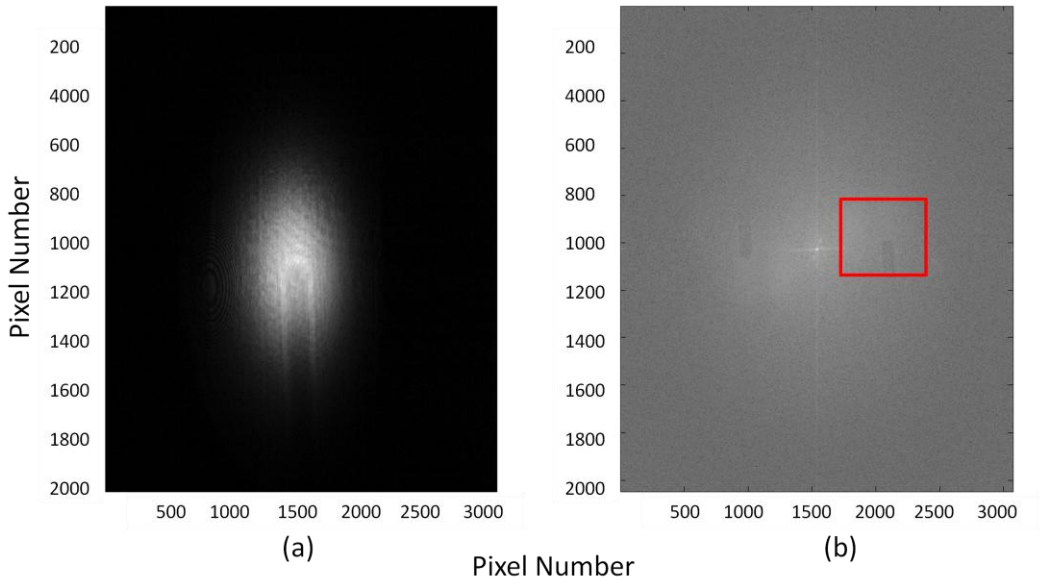

Figure 6.8: (a): The reference hologram and (b) its reconstructed image of metal rod in a cuvette of water. The red rectangle highlights the region where the real image appears in the reconstructed image.

Following the reference, heat was applied in the form of a flame to the rod as a sequence of images was taken concurrently. The phases were extracted from the reconstructed images and subtracted from the reference, and the phase difference diagrams can be seen in sequence in figure 6.9. As expected, the pattern of heating and its consequential spread is highlighted by the pattern of the wrapped modulo 2π phases which spread out around the tip of the rod (emphasised by random phases and framed by red outline on the first figure). The images were taken at the maximum frame rate of 2.4 frames per second, as allowed by the camera. The quick succession showed very little change in consecutive images but it can be determined that the phase fringes are getting closer and closer together. This should be expected, as the temperature gradient increases and therefore inducing more rapid change resulting in a more rapid phase variation.

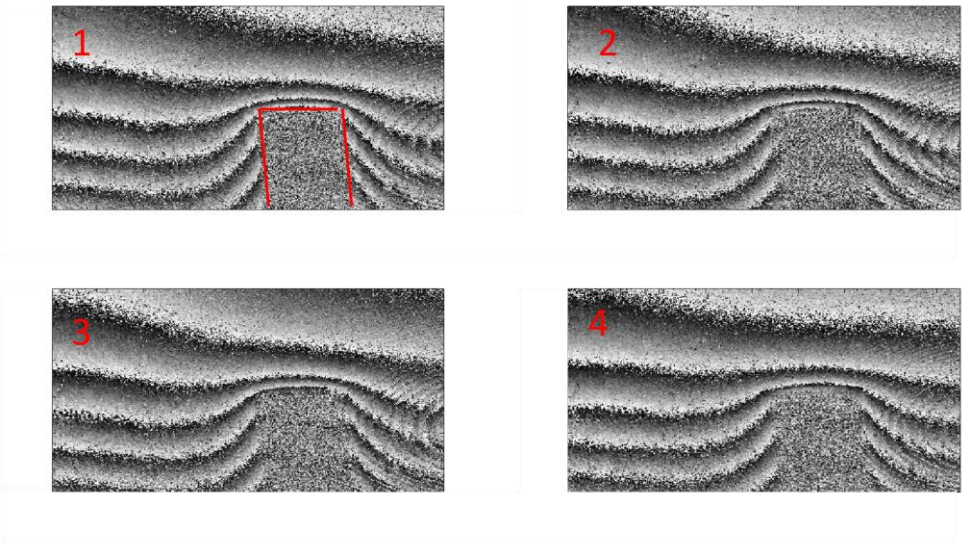

Figure 6.9: Phase difference (from the reference) images of heated water in a cuvette from a metal rod in sequence. The order of the images is as labelled. The phase differences are wrapped, as shown by the fringes of modulo 2π phases.

To make the images more meaningful, a phase unwrapper was applied to unwrap the 2π modulo phases; the result can be seen in figure 6.10. As the sequence progresses, the image gets lighter in greyscale, suggesting that the phase difference decreases due to the decreasing optical path length in response to a reduction in refractive index associated with increasing temperature, as described by the theory. However, considerable noise patterns can be observed in the images shown by random out of place regions, and can be attributed to the presence of the rod due to its opaque nature. As explained in chapter 4, the unwrapper systematically looks for patterns in the image in order to unwrap and then combine the regions to form the final image.

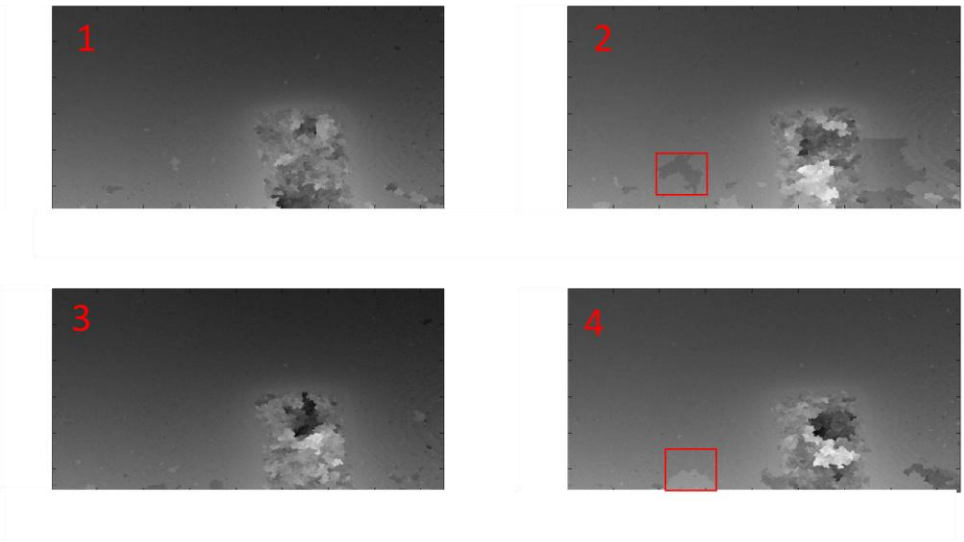

Figure 6.10: Unwrapped phase difference (from the reference) images of from figure 6.9. The order of the sequence of images is as labelled. Areas of random noise, highlighted in red boxes, due the unwrapper can be seen throughout the sequence.

A clearer phase image can be obtained by excluding the rod in the unwrapping, simply by cropping out the rod in the wrapped phase difference images from figure 6.9 before applying the unwrapping algorithm. The result can be seen in figure 6.11. As with figure 6.10, the general trend is that the images get lighter as the sequence progresses.

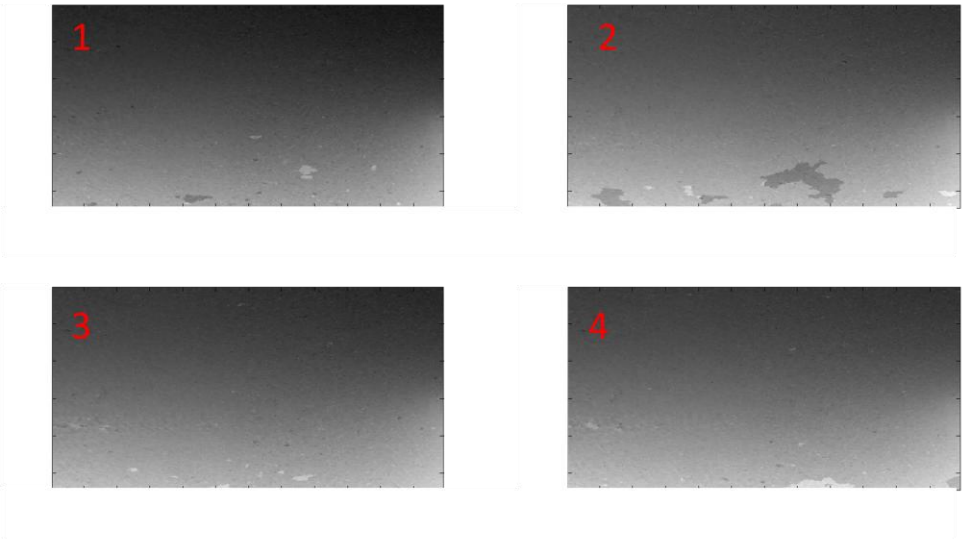

Figure 6.11: Unwrapped phase image of water heating by rod, excluding rod. The rod was cropped out from the wrapped phase images before unwrapping. The order of images as labelled.

6.2.4 Water heating with infrared laser

In the first trial, the beam output from the optical fibre was not collimated and allowed to diverge. The laser power was set at an output of 1W at 1489nm and the initial room temperature was measured to be 20.8 degrees Celsius and the final temperature of the water at the top of the cell was measured at 28.8 degrees Celsius after 20 minutes. A selected sample phase difference images of the sequence can be in figure 6.12, each image labelled according to the time it was taken. The images are inverted, as with the previous set of images. The first 2 images, at 0 and 1 minute, show almost uniform phase differences, meaning there was very little variation in the temperature. However, the latter two images at 10 and 20 minutes respectively, show a pattern of light to dark from the bottom of the image. As expected, this shows that the heating from the laser amounted to a heat gradient.

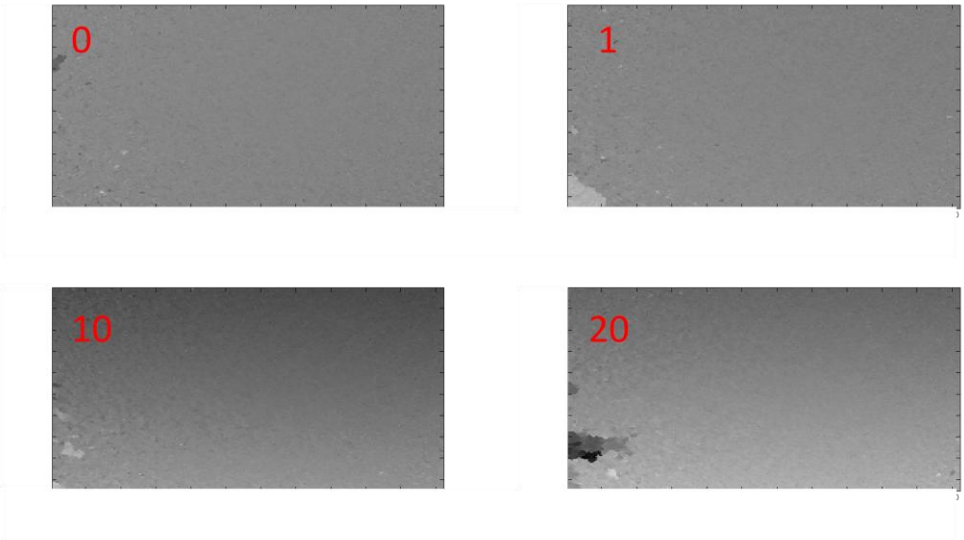

Figure 6.12: Grey-scaled phase difference images of cuvette of water heated by IR laser. Darker shade indicates a lower phase difference, whereas lighter shade indicates higher phase difference. The time (in minutes) of images is as labelled. The first two images at 0 and 1 minute show uniform phase differences; the latter two images at 10 and 20 minutes show a gradient has developed.

The phase differences were converted to temperatures according to the equations 2.32 and 2.33 in chapter 2. However, the results confirmed the temperature gradient there was a temperature gradient but in the opposite direction to what was expected, as shown by the images seen in figure 6.13. The lighter shade indicated a higher temperature whereas the darker shade indicated a lower temperature on the greyscale images. The temperatures were lower near the top of the cuvette and the temperature was higher deeper into the water sample. Also, the absolute temperature values were not expected. The temperature ranges from 19.5 to 21 degrees Celsius, which is anomalous when compared to the initial measured temperature of 20.8 degrees Celsius.

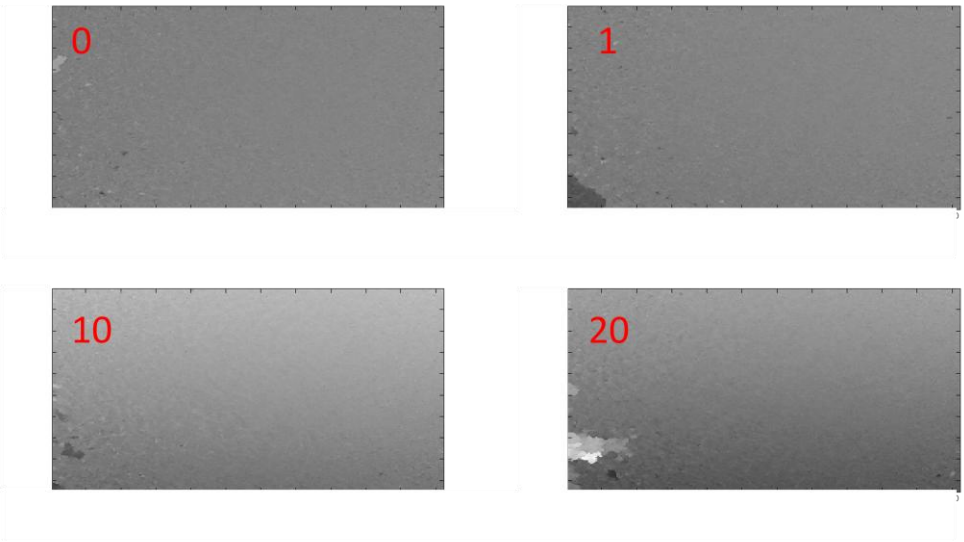

Figure 6.13: Grey-scaled temperature images converted from phase differences in figure 6.12. Darker shade indicates a lower temperature, whereas lighter shade indicates higher temperature. The time (in minutes) of images is as labelled.

To further analyse the anomaly in the series of images, a line of interest was defined from the bottom of the image to the top, as shown by the blue line in figure 6.14. Physically, this line would be from the top of the cuvette, or water surface, to the bottom of the cuvette. A profile along this line was taken and plotted, as shown in figure 6.15.

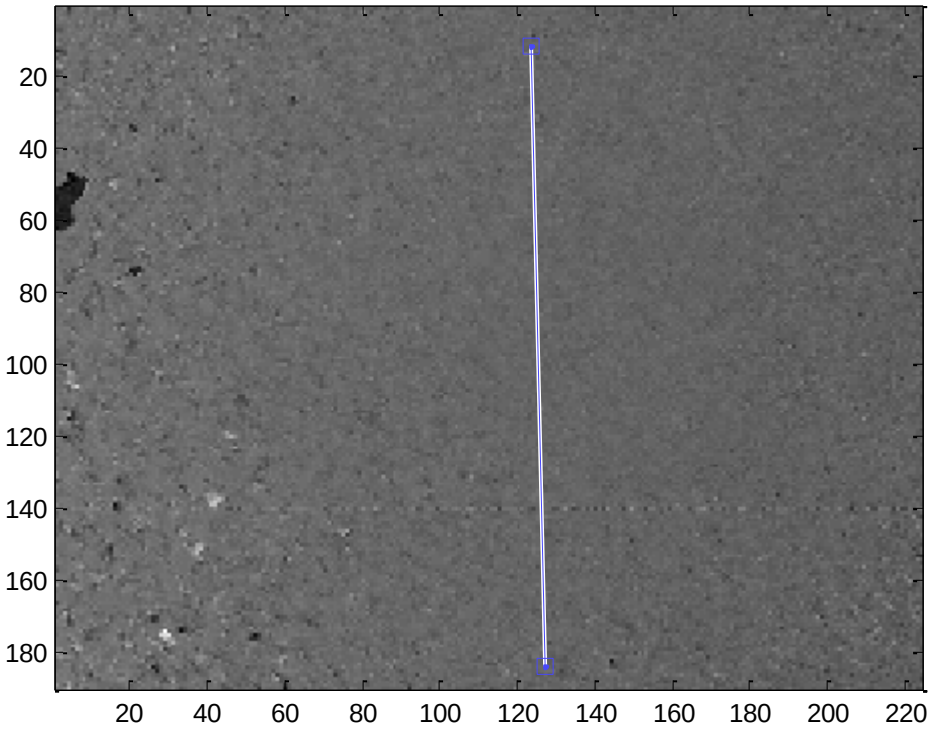

Figure 6.14: Magnified 0 minute phase difference image showing the definition of the line of interest.

The temperature profiles was consistent with the previous description where the 0 and 1 minute profiles show the temperature was within a narrow range and fairly stable. However, the latter 10 and 20 minutes profiles show that there was a steadily increasing temperature gradient, ranging from 19.5 to 21 degrees Celsius, which does not match the measured 28.8 degrees Celsius.

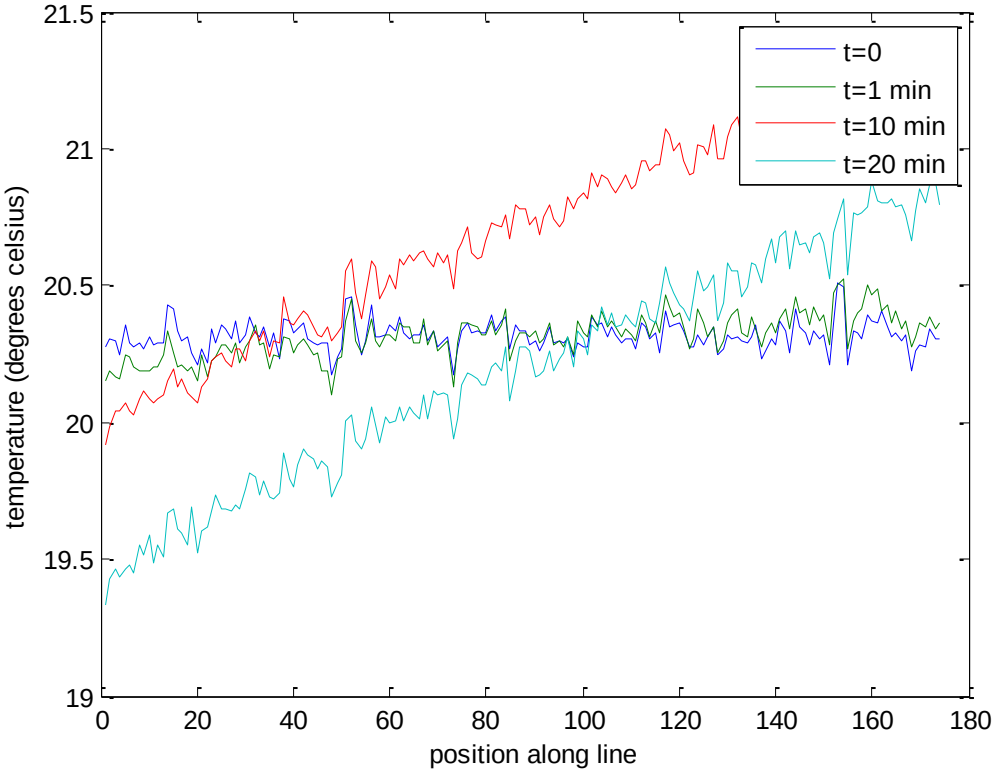

Figure 6.15: Temperature profiles along the line of interest (defined in figure 6.14). The profiles at 0 and 1 minute show relatively flat and stable temperatures; while profiles at 10 and 20 minutes show a steady gradient.

Recall that the phase differences were measured in units of the wavelength, or modulo 2π radians; and that in order to find the absolute phase differences a phase unwrapper must be applied within the image to avoid unwanted phase jumps. Essentially, this discrepancy can be attributed to this problem, but instead of phase jumps being in neighbouring pixels within the image, it is occurring in pixels over the period of time of recording.

One potential solution to this problem is to apply an unwrapper either in a three dimensional manner (two dimensions within the image and along the time dimension); or unwrap the time dimension phase differences in specific regions of interest after applying a two dimensional unwrapper within the images. However, since in dosimetry the temperature changes are not as pronounced as this type of heating, unwrapping along the time dimension may not be necessary. Assuming the maximum phase shift of 2π at room temperature of 20 degrees Celsius, this equates to a rise in temperature of 0.7 degrees which is almost 3000Gy

according to the equations given in chapter 2. This numbers dwarves most calibration techniques as well as typical radiation therapy treatments which number in tens of Grays.

The second trial used a much reduced laser power in order to better test the system response. The initial temperature of the water in the sample cuvette was 22.3 degrees Celsius and the laser was set to 300mW at 1489nm wavelength. The final temperature was 24.1 degrees Celsius. The temperature scaled images can be seen in figure 6.16 with its corresponding time labelled. Since there was very little heating the images do not show any clear heating patterns like in the previous trial. Although, the 5 minute and 20 minute images are slightly lighter in the grey scaled images indicating the temperatures in those images were definitely higher.

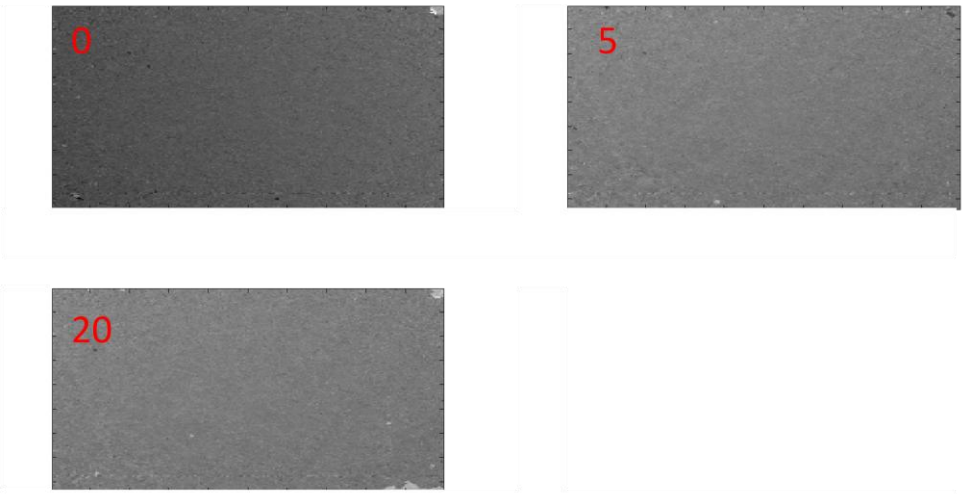

Figure 6.16: Temperature images of heated water in cuvette with labelled time in minutes. The initial 0 minute image appears darker than the 5 and 20 minute images, indicating the temperature was lower.

A line similar to that of the previous experiment was defined down the centre of the series of images and its temperature profiles are plotted and can be seen in figure 6.17. The profiles show that at 5 and 20 minutes, it hovers around 22.4 degrees Celsius, which are clearly well above the initial 0 minute profile of around 22 degrees Celsius. This confirms that the water was indeed heated by the laser and has reached steady state temperature after only 5 minutes. Another noticeable feature in the profiles is that it appears flat, indicating there was no heat gradient in the water.

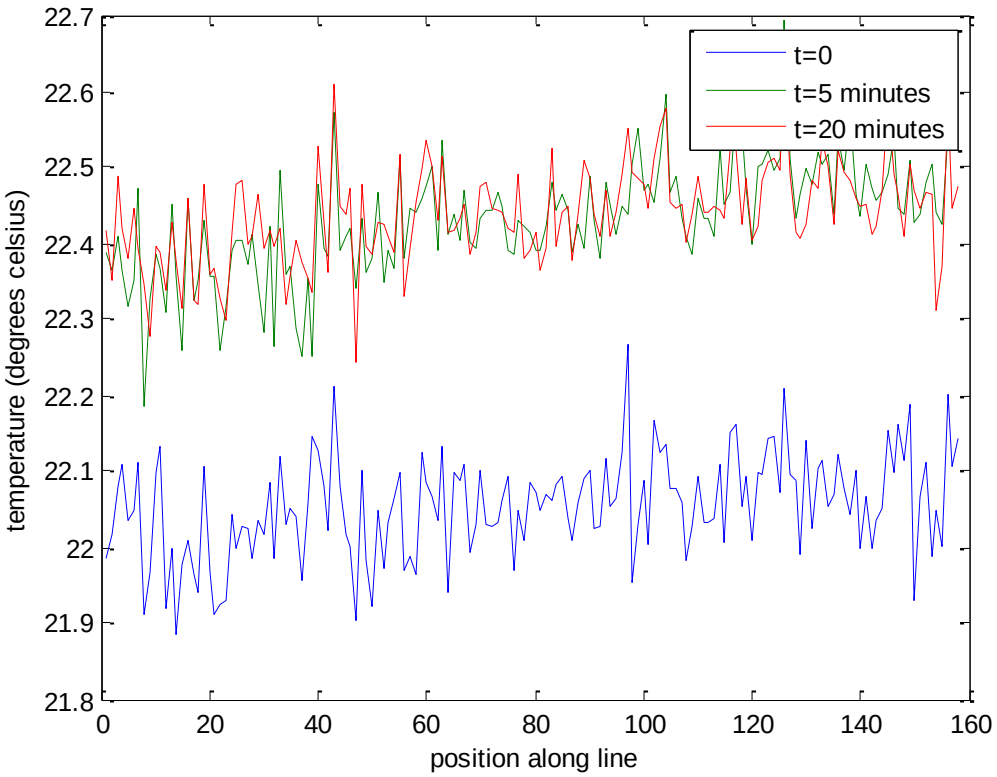

Figure 6.17: Temperature profiles along the line of interest. The profile of the initial 0 minute show relatively flat and stable temperatures; the 5 and 20 minutes profiles are also flat but at a higher temperature than the initial profile.

6.2.5 Stability

For short term stability test, an initial reference frame was taken and compared with three images taken in quick succession at one frame per second. The initial measured temperature was 24.8 degrees Celsius. An arbitrary point was selected within the reconstructed image and its converted temperature values are plotted in figure 6.18. The standard deviation was found to be 0.012.

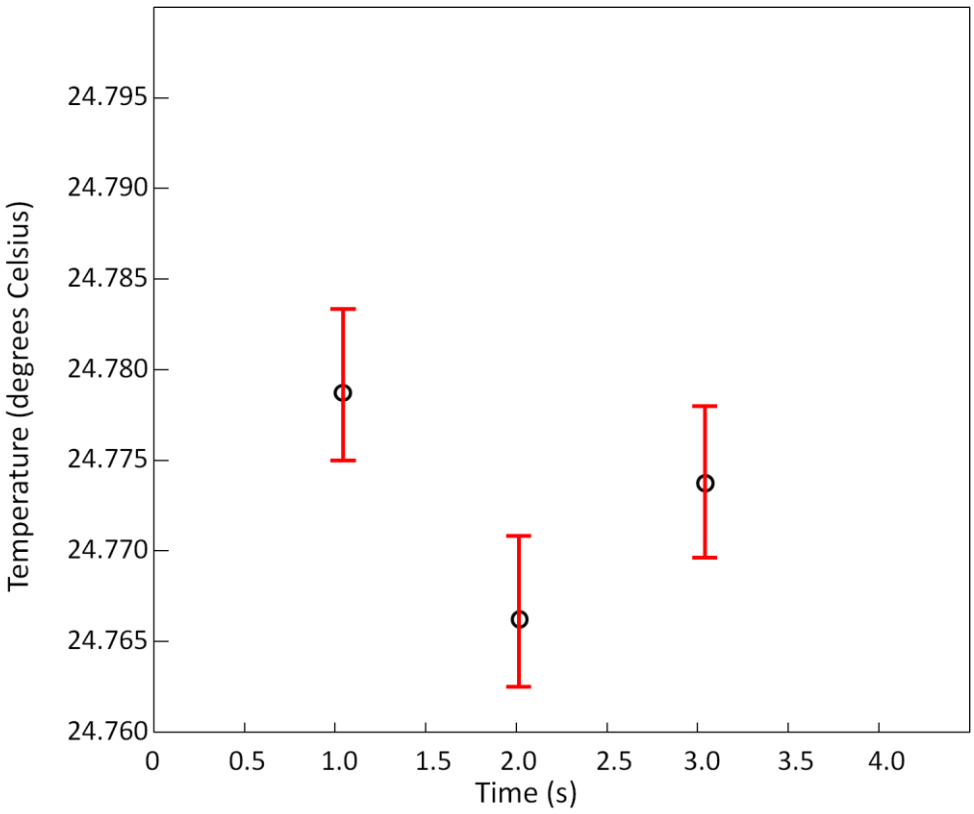

Figure 6.18: Temperature of a point with error bars over seconds during a short stability test. The standard deviation of the temperature over the time period was calculated to be 0.012 of a degree.

A long term stability test was conducted similar to the short term test above. An initial reference was taken and compared to six more images taken at one frame per minute. The initial temperature was measured to be 24.5 degrees Celsius. The final temperature was measured at 25.3 after 6 minutes, a decrease of 0.2 degrees Celsius. A point was selected within the image and its temperature traced over time, as shown in figure 6.19. The standard deviation was found to be 0.078. However, due to the variation in the ambient temperature over the experiment time period, 0.078 is a worst case scenario.

Both stability tests highlighted that the temperature variation in the setup is very low, only a small fraction of degree. But the temperature expected from a typical radiotherapy treatment is also very small. Typical treatments are approximately 70Gy, or equivalent to 0.017 of a degree in temperature change in water. The short stability test concluded with a standard deviation of 0.012 degrees, equivalent to approximately 50Gy; and in the long stability test the standard deviation was 0.078 degrees (the actual standard deviation should be lower due to decreasing ambient temperature over the experiment time) or equivalent to approximately 320Gy. The standard deviations suggest that the setup is not suitable to measure miniscule temperature changes in dosimetry.

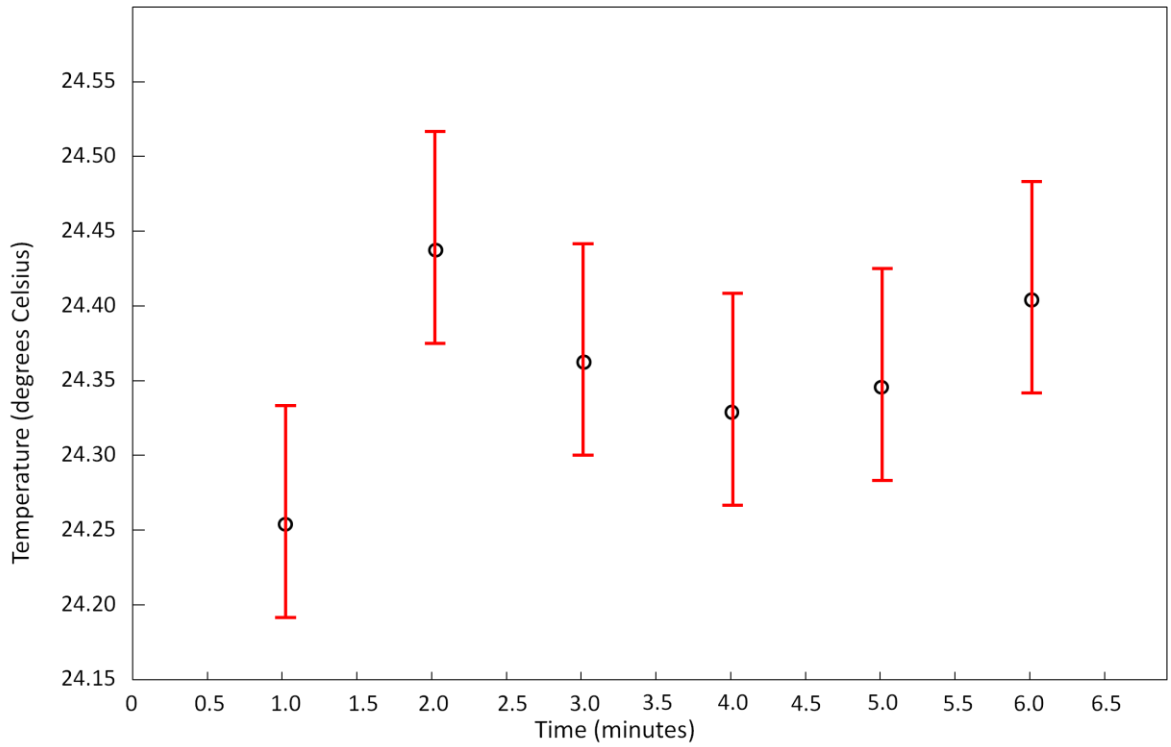

Figure 6.19: Temperatures with error bars of a point over minutes with standard deviation of 0.078. The variation of the temperature over the time period was within 0.2 of a degree.

6.3 Camera replacement

The previous sections detailed results of images captured by a CCD camera. Recall from section 4.4.5, we stated that we planned to use wave guides to direct the images away from potential high energy radiation sources, hence devised the setup utilise scanning mirrors, optical fibres and photodiode detector. In this section, we discuss the difficulties encountered when scanning mirrors and a photodiode was used in place of the camera.

6.3.1 Calibration

The galvanometer-driven scanning mirrors functioned as designed, translating the hologram image at the set frequency in both the horizontal and vertical directions as set by the input frequency generators. The image scanned across the injection stage where optical fibre end was clamped, allowing light from the image to enter the wave guide and directed towards the photodiode. The photodiode converted the light into voltage signal and passed onto the DAQ card where it would be converted into digital signals and recorded with a connected computer.

However, one major issue was that the photodiode output voltage was relatively low and not significantly above background leakage voltage in the diode. This meant that there was insufficient light reaching the photodiode. The obvious solutions were to either increase the power of the laser or improve the coupling and minimising losses throughout the setup to

allow more light reaching the detector. Since there no other laser available and the coupling were readjusted multiple times but no improvement. Due to time restriction, this detection method was not fully implemented.

6.4 Concluding remarks

In this chapter, we discussed the results obtained through various tests and experiments for each of the different setups described in chapter 5. In the next chapter, the limitations of the setup will be reviewed, followed by a conclusion of the thesis.

7. Limitations and Conclusion

In this chapter, we will discuss some of the limitations of the research, before summarising with a conclusion and possible suggestions for future work.

7.1 Limitations

The biggest challenge in this research was to extract the phase information useful in the context of dosimetry. As mentioned earlier, phases are measured by the units of wavelength (modulo 2π); and associated with this is the uncertainty in inferring the exact phase shift (wrapped phase). Since this is not a unique problem and unwrappers are widely available; one was implemented to unwrap and smooth out the phase differences within the image. However, it was restricted in a way that if the true phase difference between neighbouring pixels were greater than the set tolerance threshold (usually within $\pm\pi$), then it would be unable to discern the true phase difference. In other words, the unwrappers can only perform if there were no sudden jumps within the image. In spite of this, the aforementioned phase jumps should not occur within conventional clinic radiation dosimetry as the energy imparted forms a gentle heat gradient pattern, but it is a potential source of error for images that are taken over time. As mentioned in the laser heating experiment, the temperature did indeed exceed the 2π phase difference between snapshots and as a result the temperature was not deduced correctly. Potentially, more images can be taken within the time frame to restrict the phase differences between successive images to be within 2π, thus allowing a phase unwrapper to unwrap the true phase difference. Again, this should not be necessary in conventional clinic radiation dosimetry as 2π phase difference represents a large radiation dose in the order of thousands of Grays at room temperature. But this may prove a different case with more recent radiation dosimetry techniques with high dose rate and steep gradients such as MRT.

In the cases of high dose rate and steep gradient radiation beams, the detector or detection system's response time becomes the limitation. The detector's response time and its ability to write images onto storage memory must be able to keep the phase differences between snapshots to within the ideal 2π. The DLSR camera used in part of the experiments had very poor frame rate, and very few pictures can be taken in quick succession before the memory buffer overloaded. However, the trade off for poor frame rate was the excellent resolution (3000 x 2000 pixels) and small pixel size (7.4 x 7.4 μm).

One of the other limitations of the system was the accuracy required. A typical radiation therapy treatment might only take 70Gy, equivalent to only a fraction of degree in temperature change. The short stability test conducted showed the system at rest, the temperature

fluctuated with a standard deviation of 0.012 degrees, equivalent to approximately 50Gy; and in the long stability test the standard deviation was 0.078 degrees (the actual standard deviation should be lower due to decreasing ambient temperature over the experiment time) or equivalent to approximately 320Gy. It was limited by the amount of vibration in the system and environment, mostly due to the nearby construction site, affected the phase recordings. Steps could be taken in order to reduce the vibrations such as insulating the system and more controlled environmental conditions.

7.2 Conclusion

Throughout this research we have described how optics can be used to approach dosimetric experiments, and built setups towards this goal. In chapter 1, we briefly described some of the existing dosimetric techniques and devices currently in clinical use. Although each technique is sufficient in its ability to quantify radiation doses, however, the doses are estimates relying on calibration curves and assumptions. Also, the current techniques are not satisfactorily able to discern the dose from high dose rate and rapidly changing gradient techniques such as MRT. These shortfalls provided the motivation to look for an alternative. In chapter 2, we described the theory and mathematics behind the optical approach. From Maxwell's equation for waves we derived how light would behave when it encounters another source of the same wavelength, resulting in the interference phenomenon. Following Huygen's principle and the quantitative Fresnel-Kirchhoff integral, digital holography was explained and how the interference phase differences allowed the calculation of the change of optical path length and subsequently temperature change and how it can be converted into energy absorbed or dose. Chapter 3 discussed the practical digital holography reconstruction and steps taken for simpler image manipulation. This included the method we used to avoid the DC term overlapping with the real and virtual images by introducing an angle between the reference and sample beams. We also encountered wrapped phases and the application of a phase unwrapper in order to overcome it. Chapter 4 detailed the practical considerations of optical experimentations specific to this setup. These included the components choices such deciding on using the He-Ne laser with regards to its less absorbent wavelength and its long coherence; and also the detector type and the calculation for the resolution needed in order to meet the sampling requirement.

In chapter 5, the setups were described and various experiments designed to test certain aspects, including spatial separation; detector response; phase extraction; and heating water samples. Chapter 6 discussed the results from the experiments in chapter 5. The initial setup responded well to spatially separating the virtual image from the real image by off-axis holography. The phase test showed it was able to discern a uniform phase of the obstructing glass slide apart from the uncovered beam. The rod heating experiment in the fibre injection

setup showed that the phase differences in the images were the result of the heating, in the pattern of an outward gradient emanating from the rod. In the laser heating experiments, we could deduce the temperature and therefore energy from the change in refractive index, but only limited to phase differences within 2π, due to wrapped phases. After limiting the heat applied to ensure the phase differences to stay within 2π, we can confidently calculate the temperature change. In the stability tests, we demonstrated the accuracy of the system and found it subject to the amount of vibration in the vicinity. In the short term, a standard deviation of 0.015 degrees was recorded but a larger standard deviation of 0.078 degrees was measured in the longer term. These showed that we can be confident of the temperature measurements to be accurate within 0.1 of a degree, or equates to hundreds of Grays in radiation dose.

In summary, several setups were constructed to test the optical approach for dosimetry through the measurement of the change in the optical path length, while utilising optical fibres to avoid radiation damage to the electronic and optical components. We were able to measure temperature differences due to heating through electromagnetic radiation but found the accuracy to be insufficient for dosimetry. With further work in insulation and stability improvements, this approach could be improved and is likely useful for high dose rate applications such as MRT.

7.3 Future works

Due to time constraints, the camera replacement detection method with the photodiode was not fully implemented. While the theoretical working basis was established, further work was needed in calibrating the scanning mechanism and the light injection into the detection fibre and the photodiode.

The current limit on accuracy was imposed by the amount of vibration in the system from the surrounding environment. Insulation materials such as polystyrene foam could be incorporated into the setup in order to shield some of the unwanted vibrations.

Transportability may be another feature that should be investigated, as the setup was devised with clinical use in mind.

References

1. WHO. *WHO - Cancer.* 2011 [cited 2011 9/52011]; Available from: http://www.who.int/mediacentre/factsheets/fs297/en/.
2. Hall, E.J. and A.J. Giaccia., *Radiobiology for the Radiologist*. 6 ed. 2006: Lippincott Williams & Wilkins.
3. Pogorsak, E.B., *Radiation Oncology Physics:A Handbook for Teachers and Students*. 2005: IAEA.
4. (ICRU), I.C.o.R.U.a.M., *Fundamental Quantities and Units for Ionising Radiation (ICRU report 60)*. 1998.
5. Khan, F.M., *The Physics of Radiation Therapy*. 2010: Lippincott Williams & Wilkins.
6. Johns, H.E. and J.R. Cunningham, *The Physics of Radiology*. 1983.
7. Serduc, R., et al., *High-Precision Radiosurgical Dose Delivery by Interlaced Microbeam Arrays of High-Flux Low-Energy Synchrotron X-Rays*. PLoS ONE, 2010. **5**(2): p. e9028.
8. ESRF. *Microbeam Radiation Therapy (MRT).* 2009 11/5/2011]; Available from: http://www.esrf.eu/UsersAndScience/Experiments/Imaging/ID17/mrt-1.
9. Dilmanian, F.A., et al., *Murine EMT-6 Carcinoma: High Therapeutic Efficacy of Microbeam Radiation Therapy*. Radiation Research, 2003. **159**(5): p. 632-641.
10. Siegbahn, E.A., et al., *Dosimetric studies of microbeam radiation therapy (MRT) with Monte Carlo simulations*. Nuclear Instruments and Methods in Physics Research Section A: Accelerators, Spectrometers, Detectors and Associated Equipment, 2005. **548**(1-2): p. 54-58.
11. Abdul Rahman, A.T., et al., *The thermoluminescence response of Ge-doped silica fibres for synchrotron microbeam radiation therapy dosimetry*. Nuclear Instruments and Methods in Physics Research Section A: Accelerators, Spectrometers, Detectors and Associated Equipment, 2010. **619**(1-3): p. 167-170.
12. Crosbie, J.C. and et al., *A method of dosimetry for synchrotron microbeam radiation therapy using radiochromic films of different sensitivity*. Physics in Medicine and Biology, 2008. **53**(23): p. 6861.
13. Kreis, T., *Introduction*, in *Handbook of Holographic Interferometry*. 2005, Wiley-VCH Verlag GmbH & Co. KGaA. p. 1-8.
14. *Springer Handbook of Experimental Solid Mechanics*, ed. W.N. Sharpe. 2008: Springer.
15. Hussmann, E.K., *A Holographic Interferometer for Measuring Radiation Energy Deposition Profiles in Transparent Liquids*. Appl. Opt., 1971. **10**(1): p. 182-186.
16. Miller, A., *Holography and Interferometry in Dosimetry*. Nukleonika, 1979. **24**(9).
17. Nicolau, S., D.G. Sporea, and V.I.R. Niculescu, *Holographic interferometry in radiation dosimetry, microprocessor assisted*. 1999: p. 393-399.
18. Schnars, U. and W. Jueptner, *Digital Holography*
Digital Hologram Recording, Numerical Reconstruction, and Related Techniques. 2005.
19. Clarke, R., *CCD X-ray detectors : opportunities and challenges*. Nuclear Instruments and Methods in Physics Research Section A: Accelerators, Spectrometers, Detectors and Associated Equipment, 1994. **347**(1-3): p. 529-533.
20. LOT-Oriel, *Notes on X-ray Damage*, LOT-Oriel, Editor. 2012.
21. Hecht, E., *Optics (4th Edition)*. 2001: Addison Wesley.
22. Pedrotti, F. and L. Pedrotti, *Introduction to Optics (3rd Edition)*. 2006: Benjamin Cummings.
23. Dobbins, H.M. and E.R. Peck, *Change of refractive index of water as a function of temperature*. J. Opt. Soc. Am., 1973. **63**(3): p. 318-320.

24. Schiebener, P., et al., *Refractive index of water and steam as function of wavelength, temperature and density*. Journal of Physical and Chemical Reference Data, 1990. **19**(3): p. 677-717.
25. Mitra, S.K., N. Dass, and N.C. Varshneya, *Temperature Dependence of the Refractive Index of Water* Journal of Chemical Physics, 1971. **57**(4): p. 1798.
26. Bashkatov, A.N. and E.A. Genina, *Water refractive index in dependence on temperature and wavelength: a simple approximation*. 2003: p. 393-395.
27. Urone, P.P., *College Physics*. 2001, Pacific Grove, CA: Brooks/Cole.
28. Janda, M., I. Hanák, and V. Skala, *Holography Principles*. 2006, University of West Bohemia in Pilsen, Czech Republic.
29. Benton, S.A. and V.M. Bove, *Off-Axis "Leith & Upatnieks" Holography*, in *Holographic Imaging*. 2007, John Wiley & Sons, Inc. p. 103-113.
30. Leith, E.N. and J. Upatnieks, *Reconstructed Wavefronts and Communication Theory*. J. Opt. Soc. Am., 1962. **52**(10): p. 1123-1128.
31. Gdeisat, M. and F. Lilley, *Two-Dimensional Phase Unwrapping Problem*.
32. Pritt, M.D., C.G. Dennis, and D.C. Ghiglia, *Two-dimensional phase unwrapping : theory, algorithms, and software / Dennis C. Ghiglia, Mark D. Pritt*. 1998: New York : Wiley, c1998.
33. Herráez, M.A., et al., *Fast two-dimensional phase-unwrapping algorithm based on sorting by reliability following a noncontinuous path*. Applied Optics, 2002. **41**(35): p. 7437.
34. Chaplin, M. *Water Absorption Spectrum*. Water Structure and Science 2012 29/7/2012 [cited 2012 2/10/2012]; Available from: http://www.lsbu.ac.uk/water/vibrat.html.
35. Canon. *Canon EOS 300D*. 2/10/2012]; Available from: http://www.canon.co.uk/for_home/product_finder/cameras/digital_slr/eos_300d/.
36. *Optical Couplers - Special Wavelengths 532 630 830 980 1064 1480*. 2012; Available from: http://www.oemarket.com/product_info.php?cPath=23&products_id=77.
37. *Model 6215H Moving Magnet Closed Loop Galvanometer Based Optical Scanner*. 2012; Available from: http://www.camtech.com/products/6200/6215.html.
38. *Servo Driver MicroMax® 671XX Single Axis*. 2012; Available from: http://www.camtech.com/Products/servos/Servo%20Driver-671XX.html.
39. *DET10A - Si Detector*. 2012; Available from: http://thorlabs.com/thorProduct.cfm?partNumber=DET10A.
40. *USB-1608FS*. 2012; Available from: http://www.mccdaq.com/usb-data-acquisition/USB-1608FS-Plus.aspx.

Appendix A

Matlab reconstruction script

```
Recon.m           Kaidi Liang 2011
%Partially taken from dhi10KL.m
%7/11/2011

clc
clear all
close all

d = 360e-3;                                          %distance between
object and detector
lambda = 632.8e-9;                                   %wavelength
ds = 7.4e-6;                                         %detector size
c1 = (1i/(lambda*d));                                %constants used in
the reconstruction
c2 = (exp((-1i*2*pi*2*d/lambda)));
c3 = (-1i*pi/(lambda*d));


%% Load holograms h1, h2
[filename1, pathname1] = uigetfile( ...
    {'*.tif';'*.jpg'}, ...
    'Pick reference hologram');
cd(pathname1)
% Consecutive hologram(s)
[filename2, pathname2] = uigetfile( ...
    {'*.tif';'*.jpg'}, ...
    'Pick second hologram',...
    'MultiSelect', 'on');

% are multiple holograms selected?
if iscell(filename2) % more than 1 files selected
    multiple ='y';
    disp(['Sequence of ',num2str(length(filename2)), ' holograms
selected.'])
    filename2=sort(filename2); % sort as uigetfile returns files in
arbitrary order
    num_iterations = length(filename2);
else
    multiple='n';
    num_iterations = 1;
end

%% Reconstruction ref

img = double(imread(filename1));
img = img(:,:,1) + img(:,:,2) + img(:,:,3); %if RGB

s = size(img);
offset = s/2 + 1;

ft_img = fftshift(ifft2(img));
```

```
for n=1:s(1,1);                     %loop to run position dependent
reconstruction
    for m=1:s(1,2);
        image(n,m) = c1 * c2 * (exp(c3*((((n-offset(1))*ds)^2)+(((m-
offset(2))*ds)^2)))) * ft_img(n,m);
    end
end

colormap('gray')                    % log so ROI can be visualised
imagesc(log(abs(image)))
title('Log of absolute of interferogram - Select ROI and double click -
then wait...')
axis tight equal

h = imrect;                         % select Region of Interest (ROI)
position = wait(h);                 % Interactively place a rectangle by
clicking ...
                                    % and dragging. Use wait to block the
MATLAB command line.
                                    % Double-click on the rectangle to
resume

pos=round([position(1) position(2) position(1)+position(3)
position(2)+position(4)]) % xlow ylow xhigh yhigh

ref_phase = (angle(image(pos(2):pos(4), pos(1):pos(3))));  %phase for a
specific region of interest

%% Reconstruction obj

% holog_i=2
for holog_i=1:length(filename2);

    %disp(['Reconstructing hologram ',num2str(holog_i),
'/',num2str(num_iterations),' (',char(filename2(holog_i)),')...'])
    img = double(imread(char(filename2(holog_i)))); % hologram 2
    img = img(:,:,1) + img(:,:,2) + img(:,:,3); %if RGB

    s = size(img);

    ft_img = fftshift(ifft2(img));

    for n=1:s(1,1);                                 %loop to run
position dependent reconstruction
        for m=1:s(1,2);
            image(n,m) = c1 * c2 * (exp(c3*((((n-offset(1))*ds)^2)+(((m-
offset(2))*ds)^2)))) * ft_img(n,m);
        end
    end

    obj_phase = (angle(image(pos(2):pos(4), pos(1):pos(3))));   %phase
for a specific region of interest

    % Phase difference

    t = size(obj_phase);

    for n = 1:t(1,1)
        for m = 1:t(1,2)
            if  ref_phase(n,m) >= obj_phase(n,m);
```

```
                phase_diff(n,m) = ref_phase(n,m) - obj_phase(n,m);
            else
                phase_diff(n,m) = ref_phase(n,m) - obj_phase(n,m) + 2*pi;
            end
        end
    end

    unwrapped_phase_diff(:,:,holog_i) =
Miguel_2D_unwrapper(single(phase_diff)); %Miguel et al unwrapper

%     fOut = sprintf('phase%d.txt', holog_i);
%     dlmwrite(fOut, unwrapped_phase_diff);


end

%% Temp and dose
T_i = 23.4;          %Initial temperature
n_20 = 1.332156;      %RI at 20 deg C
n_i = (-8.889*(T_i -20) - 0.1610*((T_i-20).^2))/1e5 + n_20;      %Dobbins
et al n v T fit
dn = lambda * unwrapped_phase_diff / (2*pi*0.01);                %change
in RI from change in path length
n_f = n_i + dn;

T_f = ((-8.889 + sqrt((8.889.^2)-(4*0.1610*((n_f-
n_20)*10.^5))))/(2*8.889)) + 20;   %Quadratic formula to find temperature
from RI
dT = T_f - T_i;

dose = 4185.5 * dT;          %finding dose from specific heat for water
and change in temp
```